Perfusion-dependent spreading depolarization signatures identify tissue vulnerability in stroke

Samuel M. Flaherty,[1,2,3] Ahmed Eladly,[1] Kate Hills,[1] Jill Merlini,[2,3] Lorena F. Fernandes,[1,2,3] Eduard Masvidal-Codina,[4,5] Xavi Illa,[5,6] Elisabet Prats-Alfonso,[5,6] Elena Del Corro,[4] Jose A. Garrido,[4,7] Jannis Meents,[8] Christoph Jeschke,[8] Rainer Mohrlok,[8] Kostas Kostarelos,[1,3,4,7,9] Stuart M. Allan,[2,3] Anton Guimerà-Brunet[5,6] and Robert C. Wykes[1,2,3,10]

Abstract

Cortical spreading depolarizations (CSDs) are large-scale disruptions of neuronal homeostasis that contribute to secondary injury after ischaemic stroke and occur across a range of acute and chronic neurological disorders. In healthy cortex, CSDs are typically coupled to compensatory vasodilation, whereas in ischaemic tissue they can evoke inverse haemodynamic responses that exacerbate metabolic stress and promote lesion progression, highlighting the need for approaches that can resolve localised electrophysiological and vascular dynamics as a function of evolving tissue metabolic state.

Here, we combine high-density graphene micro-transistor arrays with optical cerebral blood flow and oxygenation imaging to map perfusion-dependent electrophysiological and haemodynamic dynamics of CSDs during focal cerebral ischaemia. Using two complementary stroke models, we show that CSD waveform duration and morphology scale systematically with local perfusion gradients, revealing distinct electrophysiological signatures that reflect tissue metabolic state. These signatures resolve a continuum from relatively preserved cortex to markedly ischaemic regions within a single preparation. We identify a characteristic CSD waveform that precisely localises profoundly hypoperfused tissue and demonstrate that specific electrophysiological features predict whether a given CSD will elicit vasodilatory, biphasic, or vasoconstrictive haemodynamic responses.

Using neural network modelling, we further show that DC-coupled electrophysiology alone can accurately predict local vascular responses to CSDs, indicating that critical information about tissue state and neurovascular risk is encoded within the CSD waveform itself in these models. Concurrent oxygenation imaging reveals a focal pre-onset decline in tissue oxygenation at sites of CSD initiation and shows that prolonged CSDs impose

© The Author(s) 2026. Published by Oxford University Press on behalf of The Guarantors of Brain. This is an Open Access article distributed under the terms of the Creative Commons Attribution License (https://creativecommons.org/licenses/by/4.0/), which permits unrestricted reuse, distribution, and reproduction in any medium, provided the original work is properly cited.

ACCEPTED MANUSCRIPT

Downloaded from academic.oup.com/brain/advance-article/doi/10.1093/brain/awag305/8788779 by guest on 24 November 2026

sustained metabolic burden, linking electrophysiological dynamics to tissue oxygen recovery.

Finally, we demonstrate that low-dose ketamine shortens CSD duration, thereby preventing the inverse haemodynamic response in metabolically compromised tissue, providing a physiological mechanism for its reported neuroprotective effects.

Together, these findings establish perfusion-dependent CSD signatures as high-fidelity functional biomarkers of tissue state and neurovascular risk, enabling real-time delineation of severely compromised, at-risk, and relatively preserved cortex. While demonstrated here in ischaemic stroke, this framework has broad relevance for monitoring injury evolution and therapeutic response in neurological disorders where spreading depolarizations play a pathogenic role.

Author affiliations:

1 Centre for Nanotechnology in Medicine, University of Manchester, Manchester, M13 9PL, UK

2 Division of Neuroscience, School of Biological Sciences, Faculty of Biology, Medicine and Health, The University of Manchester, Manchester Academic Health Science Centre, Manchester, M13 9PL, UK

3 Geoffrey Jefferson Brain Research Centre, Manchester Academic Health Science Centre, Northern Care Alliance NHS Foundation Trust, University of Manchester, Manchester, M6 8HD, UK

4 Catalan Institute of Nanoscience and Nanotechnology (ICN2), CSIC and The Barcelona Institute of Science and Technology (BIST), Campus UAB, Bellaterra, Barcelona, 08193, Spain

5 Centro de Investigación Biomédica en Red en Bioingeniería, Biomateriales y Nanomedicina (CIBER-BBN), Madrid, 28029, Spain

6 Institut de Microelectrònica de Barcelona, IMB-CNM (CSIC), Esfera UAB, Bellaterra, 08193, Spain

7 Institució Catalana de Recerca i Estudis Avançats (ICREA), Barcelona, 08010, Spain

8 Multi Channel Systems MCS GmbH, Reutlingen, 72770, Germany

9 Institute of Neuroscience, Universitat Autònoma de Barcelona, Barcelona, 08193, Spain

ACCEPTED MANUSCRIPT

Downloaded from academic.oup.com/brain/advance-article/doi/10.1093/brain/awag305/8788779 by guest on 24 November 2026

10 Research Department of Epilepsy, UCL Queen Square Institute of Neurology, London, WC1N 3BG, UK

Correspondence to: Robert Wykes

Division of Neuroscience, School of Biological Sciences, Faculty of Biology, Medicine and Health, The University of Manchester, Manchester Academic Health Science Centre, Manchester, M13 9PL, UK

E-mail: rob.wykes@manchester.ac.uk

Correspondence may also be addressed to: Anton Guimerà-Brunet

Institut de Microelectrònica de Barcelona, IMB-CNM (CSIC), Esfera UAB, Bellaterra, 08193, Spain

E-mail: anton.guimera@imb-cnm.csic.es

Keywords: spreading depolarization; ischaemic stroke; ketamine; cerebral blood flow; neurocritical care; graphene

Introduction

Cortical spreading depolarizations (CSDs) are large, transient disruptions of neuronal and glial membrane potentials that propagate slowly through the cortex. First described by Leão in 1944 [1], CSDs are initiated in metabolically stressed but still viable brain tissue and are a hallmark of acute brain injury, particularly following focal cerebral ischaemia [2,3]. Across diverse neurological conditions including traumatic brain injury, subarachnoid haemorrhage, migraine aura, glioblastoma and epilepsy, CSDs emerge as an important pathophysiological process that imposes metabolic stress. CSD waves are characterised by near-complete breakdown of ionic homeostasis, resulting in neuronal and astrocytic depolarization, dendritic swelling, and spine distortion [4,5]. Recovery from a CSD is energy-intensive, requiring ATP-dependent ion pumps to restore ionic gradients, a process that is feasible in healthy tissue but significantly impaired in ischaemic regions with reduced metabolic capacity [3,6].

ACCEPTED MANUSCRIPT

Downloaded from academic.oup.com/brain/advance-article/doi/10.1093/brain/awag305/8788779 by guest on 24 November 2026

CSDs have been implicated as a key mechanism driving lesion development and progression in ischaemic stroke [2]. In both the core and the penumbra, CSDs precede the development of cell death. In the penumbra, recurrent spontaneous CSDs occurring after the initial CSD further exacerbate tissue damage and correlate with infarct expansion. [7–9]. Rather than the expected hyperaemic response seen in healthy brain, CSDs in the ischaemic cortex can trigger prolonged vasoconstriction and hypoperfusion, a phenomenon termed "spreading ischaemia" [10–13]. This inverse haemodynamic response impairs repolarization and promotes a pathological feedback loop of repeated CSDs, calcium overload, and neuronal injury [14–16,2]. Clustered CSDs pose a huge metabolic challenge for recovery and are thought to play a significant role in early cell death and lesion expansion. These observations suggest that CSD waveform properties and their associated vascular responses may encode information about local tissue metabolic state and vulnerability to secondary injury.

Determining whether CSD waveform properties correlate with localised tissue health and lesion progression in real time requires high-density, DC-coupled recordings free from attenuation and distortion. However, high resolution electrographic mapping of CSDs remains technically challenging. Conventional electrode systems, even those capable of DC-coupled recordings, are limited by drift, electrode impedance, and poor spatial fidelity [17–19]. Graphene-based solution-gated field-effect transistors (gSGFETs) offer a promising alternative. The intrinsic material properties of graphene; chemical inertness, flexibility, and high field-effect make gSGFETs well-suited for capturing the DC voltage shifts associated with CSDs [20–22]. These active transducers detect local voltage changes as current fluctuations across a graphene channel, enabling stable and wide-band recordings (Fig. S1Ai-ii). Using thin-film microelectronic technology, flexible arrays of gSGFETs can be fabricated, with a total thickness in the few micrometers range, therefore allowing correlation of localised electrographic parameters with regional cerebral blood flow (rCBF) changes directly underneath each transistor (Fig. S1C & S5).

The primary aim of this study was to determine whether high-density DC-coupled mapping of CSDs yields quantitative waveform features that predict local perfusion state and the associated haemodynamic response. Furthermore, we sought to determine whether ketamine can modulate these neurovascular dynamics by suppressing CSD-associated vasoconstriction during early focal ischaemia.

In this study, we use 16 or 30 channel epicortical gSGFET arrays (Fig. S1Bi-iii) for DC-coupled recordings in two established preclinical models of focal cerebral ischaemia: the photothrombotic (PT) [23] and the distal middle cerebral artery occlusion (dMCAo) [24] models. The use of both approaches strengthens the generalisability of our conclusions. The PT

ACCEPTED MANUSCRIPT

Downloaded from academic.oup.com/brain/advance-article/doi/10.1093/brain/awag305/8788779 by guest on 24 November 2026

model provides a reproducible, well-controlled cortical lesion with sharply defined perfusion gradients, enabling systematic mapping of CSD waveforms across regions of differing tissue viability. In contrast, dMCAo produces a more heterogeneous and spatially variable perfusion deficit. The application of two complementary models together reflects the broad clinical spectrum of human stroke.

We find that CSD duration and waveform shape scale systematically with underlying perfusion gradients, providing electrophysiological biomarkers that reflect local tissue health. These electrophysiological signatures can predict the perfusion state as well as the CSD associated haemodynamic response, distinguishing CSDs that induce vasodilation from those that trigger vasoconstriction. Using a neural network model, we demonstrate that CSD induced haemodynamic responses can be accurately predicted from DC-coupled electrophysiological recordings alone in these models. We further investigate the spatially resolved impact of CSDs on tissue oxygenation and characterise the complex spatiotemporal dynamics underlying these responses.

Using this integrated platform, we evaluated the capacity of systemic ketamine to modulate CSD during early stroke evolution. Consistent with its known ability to block or modulate CSDs in both preclinical [25–31] and clinical [32–35] settings, ketamine shortened CSD duration and converted inverse haemodynamic responses into vasodilation within metabolically compromised tissue. These findings offer a mechanistic basis for the neuroprotective effects of ketamine in the post stroke brain and highlight the utility of local DC-coupled mapping for real-time assessment of therapeutic interventions.

Materials and methods

Animals

Male and female C57BL/6J mice (10-12 weeks, 19-25g) were obtained from Envigo, UK and co-housed in ventilated cages, on a 12 h/12 h dark/light cycle, with food and water provided *ad libitum*. Animal procedures were conducted in accordance with the United Kingdom Animal (Scientific Procedures) Act 1986 and were approved by the local animal Welfare and Ethical Review Board and the Home Office. A total of 47 C57BL/6 mice were used in the described experiments. For all procedures, mice were weighed before being anaesthetized using 4% gaseous isoflurane (100% w/w; 988-3245, Henry Schein, USA) and medical gas (70% NO_2 and 30% O_2). Mice were then placed into a stereotaxic frame (David Kopf Instruments Ltd, USA). Lubrithal

ACCEPTED MANUSCRIPT

Downloaded from academic.oup.com/brain/advance-article/doi/10.1093/brain/awag305/8788779 by guest on 24 November 2026

(Dechra, UK) was applied to each eye and pain relief, consisting of a subcutaneous Buprenorphine (0.03 mg/ kg, Ceva, France) injection and topical Emla cream (5% lidocaine/ prilocaine) (Aspen, UK) were administered. Iodine was applied to the surgical area. Anaesthesia was maintained using 1.5-2% isoflurane and medical gas was provided throughout the surgical and recording period. A rectal probe and heating pad was used to maintain an internal body temperature of 37ºc. An incision was made down the midline and the skin retracted. The connective tissue was removed and the surface of the skull cleaned with saline and dried.

Craniotomy surgery

The target region was identified using skull landmarks referenced to the sagittal suture and bregma intersect. A craniotomy was performed posterior to the coronal suture at bregma and extended 3 mm posteriorly, with the medial edge placed 1.0 mm lateral to the midline suture to expose the right somatosensory cortex. The area was soaked in artificial cerebrospinal fluid (aCSF; mM concentrations in 500 ml distilled H_2O: 125 NaCl, 4 KCl, 10 glucose, 10 HEPES, 2 $CaCl_2$, 2 $MgCl_2$, achieving a constant pH of 7.35). The underlying dura was left intact.

Photothrombosis Induction of Focal Cerebral Ischaemia

Photothrombosis was induced using a 561 nm laser (CL561-050, CrystaLaser, USA) with a power output of 50 mW before fibre and 35.5 mW at the fibre tip (PM16-130, Thor Labs, NJ, USA). An optic fibre cable (ThorLabs, M128L01, 400 µm, USA) was positioned (AP: 1.0, ML: – 1.0) 0.5 mm from the epidurally placed gSGFET array. While the fibre core diameter was 400 µm, the effective illumination area was larger due to lateral light scatter and leakage around the fibre tip, as no blackout material or a collimator was used to restrict the beam. This broader illumination footprint is consistent with the infarct size. Five minutes prior to illumination, the photosensitive dye rose bengal (Sigma, UK), dissolved in saline solution (15 mg/ml), was administered by intraperitoneal injection at a dose of 150 mg/kg. The cortex was locally illuminated for an initial 60 seconds (s) period, which reliably induced a CSD. After full recovery of high frequency activity and the return of rCBF to baseline (typically 20 min), the cortex was illuminated, in the same area, for a further 180 s. The optic fibre was then removed from the preparation and electrographic and CBF monitoring continued for ~2 hours (Fig. 1Ai).

ACCEPTED MANUSCRIPT

Downloaded from academic.oup.com/brain/advance-article/doi/10.1093/brain/awag305/8788779 by guest on 24 November 2026

Pharmacological CSD modulation

The therapeutic study consisted of two groups, group 1: IP Injection of saline (n = 15) and group 2: IP injection of ketamine (15 mg/kg) dissolved in saline solution (n = 14). Therapeutics were administered 5 s prior to the second 180 s illumination. This therapeutic time window is not directly translatable to the clinical setting however the main therapeutic aim of this work was to determine the effect of ketamine on CSD waveform characteristics and the associated haemodynamic responses. As CSDs could be reliably evoked during and following the illumination periods, this temporal window was selected to maximise the experimental effect of ketamine.

Distal Middle Cerebral Artery Occlusion (dMCAo)

A straight vertical incision was made centrally between the ear and eye and the skin retracted to expose the underlying tissue/ muscle. The muscle underneath the suture line was superficially cut, detached from the skull, and retracted. The tissue covering the skull surface was removed and the area cleaned with saline. A 0.5 x 0.5 mm craniotomy was performed over the distal middle cerebral artery bifurcation. The dura was left intact. Iron (III) Chloride (Sigma, UK) was dissolved in sterile water to form a 40% concentration solution (0.4g/ml). Filter paper was soaked in the ferric chloride and placed directly onto the bifurcation of the vessel for 5 mins. Occlusion was confirmed visually, by electrographic biomarkers and by a rapid perfusion decrease (~50% perfusion change) in the laser speckle contrast imaging (Fig. S3).

gSGFET Arrays

Flexible epidural neural probes (~10 μm in thickness) containing an array of 16 or 30 graphene micro-transistors were used. Sixteen-channel (4 × 4 array, 400 μm separation between transistors) and 30 channel (5x6 array, 500 μm horizontal and 450 μm vertical separation between transistors) arrays were used (Fig S1Bi-ii). gSGFET arrays were fabricated at the clean room facilities of IMB-CNM[20]. See Supplementary Materials and Methods for additional details on gSGFET array fabrication[36].

Electrophysiological Recordings

Electrophysiological recordings were performed using flexible gSGFETs arrays. The tail of the array was inserted into a zero-insertion force (ZIF) connector on a printed circuit board (PCB) and lowered onto the dura using a micromanipulator. Signal acquisition and amplification was performed using the Multichannel systems (MCS) ME2100 in vivo system (Multi Channel Systems MCS GmbH Germany). The MCS system required a custom made GE2100, gSGFET compatible, headstage (pre-amp). Wideband signals were acquired at

ACCEPTED MANUSCRIPT

Downloaded from academic.oup.com/brain/advance-article/doi/10.1093/brain/awag305/8788779 by guest on 24 November 2026

5000 Hz and 24-Bit. Prior to recording, $I_{ds} - V_{gs}$ curves were obtained at the start and end of experiments to determine the performance of the gSGFET array. A V_{gs} bias was selected at a voltage where transconductance was most optimal (steepest point of the $I_{ds} - V_{gs}$ curve). Subsequent interpolation of acquired current signals into the transfer curve results in DC-coupled voltage signals (Fig. S1Ai)[20]. A reference wire (Ag/$AgCl_2$) was placed in the neck muscle. During electrophysiological recording, the heating blanket was turned off and a pre-heated (37°c) Deltaphase isothermal pad (Braintree Scientific, USA) was used to maintain the body temperature

LSCI and Blood Oxygenation Monitoring

A Moor Instruments moorFLPI-2 Laser Speckle Contrast Imager (Moor Instruments, United Kingdom) was used for CBF monitoring. The camera was focused onto the craniotomy and gSGFET array. The imaging field consisted of the right hemisphere, the midline and lambda. Images were acquired at 1 Hz with a 2064 x 1544 resolution. All CBF data was normalised to a stable reference point prior to ischaemia induction in each experiment. The reference point was therefore considered 100% baseline, where 1 PU is equal to the baseline. In a subset of animals, simultaneous CBF and blood oxygenation imaging was performed using the above protocol however acquired with the moorO2Flo (Moor Instruments, United Kingdom) imager. A read out of relative changes in oxygenated haemoglobin (HbO) and deoxygenated haemoglobin (HbR) was acquired.

Electrophysiology Data Analysis

Acquired electrophysiology recordings were analysed using Python 3.9 packages (Matplotlib 3.5.1, Numpy 1.21.5, Pandas 1.4.2, Seaborn 0.11.2, Neo 0.8.0) and the custom library PhyREC 0.5.3. Transistor recordings were calibrated by interpolating the current signals into the corresponding branch of the *in vivo* measured transfer curve[20]. During recording calibration, down sampling was applied by a factor of 20. A full wideband signal is acquired in the experiment. In post-analysis, raw signals were filtered into 2 separate traces, the AC-ECoG component, and the DC-ECoG component. The AC-ECoG component was bandpass filtered 1 - 45 Hz. The DC-ECoG component was lowpass filtered < 1 Hz.

ACCEPTED MANUSCRIPT

Downloaded from academic.oup.com/brain/advance-article/doi/10.1093/brain/awag305/8788779 by guest on 24 November 2026

CSD Event Detection

Semi-automated detection of CSD events was developed for this work, using Python scripts, to assist the analysis of large, multichannel, datasets. A bandpass filtered (0.05 – 0.001 Hz) signal derivative was applied to the DC-ECoG trace. At infraslow frequencies, only large voltage shifts (> 4 mV) in the DC-ECoG trace would cause large deflections in a 0.05 – 0.001 Hz bandpass filtered signal derivative (Fig. S7Ai-ii). This method of CSD event detection requires stable recordings without severe voltage drifts. We calculated the absolute voltage drift of a channel recording from tissue with no perfusion deficit (2.65 ± 1.54 mV/hr, $n = 40$; (Fig. S6A) avoiding the DC shift effects of ischaemia (I.e., presence of an NUP). The minimal DC drift highlights the impressive stability of the gSGFET arrays (Fig. S6B). Wideband recordings acquired with gSGFET arrays display impressive stability (Fig. S1Aii) that enabled the successful implementation of CSD event semi-automation to the DC-ECoG component (<0.1 Hz). All detected CSD events were manually checked before moving to the next step of the data analysis pipeline.

CSD Parameter Extraction

The onset of an CSD was defined as the onset of a steep negative DC shift with a minimum amplitude threshold of −4 mV. For each CSD event, per transistor channel, the following parameters were extracted: maximum CSD amplitude, CSD duration, and CSD depolarization speed (Fig. S7Bi-ii). Maximum amplitude was defined by the peak voltage change from the baseline as an absolute voltage. CSD duration calculation commenced when the DC-ECoG voltage decreased below -4 mV and finished when the signal recovered above -4 mV. CSD depolarization speed was calculated by quantifying the slope of the DC shift (Fig. S7Ci-ii). Python code available upon request.

Deep convolutional neural network model

Deep learning was used to support time-series classification directly from raw DC-coupled electrophysiology without feature engineering, consistent with established approaches for time-series modelling [37]. A deep convolutional neural network model was trained to predict

ACCEPTED MANUSCRIPT

Downloaded from academic.oup.com/brain/advance-article/doi/10.1093/brain/awag305/8788779 by guest on 24 November 2026

the CSD-induced haemodynamic response (vasoconstriction, biphasic, or vasodilation) from corresponding DC-ECoG (<0.1 Hz) recordings. A total of 150 CSD events and their associated haemodynamic responses were individually inspected and manually annotated for training the network. The data used to train the neural network was chosen such that all three types of haemodynamic responses were equally present. Voltage traces for each event were standardized and the following predictors incrementally added: DC-ECoG 1st derivative, DC-ECoG 2nd derivative, CSD progression index (CPI) and CSD duration.

CPI is an ordinal label assigned to each CSD event to indicate temporal order following PT induction. Specifically, for each experiment, detected CSDs were ordered chronologically and assigned CPI values of 0, 1, 2, 3, ..., N, where CPI = 0 corresponds to the first detected CSD after induction and CPI = N corresponds to the final detected CSD in that recording. CPI was assigned per event (not per channel), and the same CPI value was applied across all channels corresponding to that CSD event. No time windowing, normalization, or additional transformations were applied. Further details regarding model implementation are provided in the Supplementary Materials and Methods.

Analysis and Statistics

GraphPad Prism 10.4 software was used to perform statistical analysis. Statistical tests are described in the figure legends or results text (mean ± sd). Data normality was assessed prior to the application of statistical tests. Pairwise comparisons were performed using two-sided unpaired *t*-tests. Data sets greater than two groups were compared using either one-way ANOVA or two-way ANOVA. A Spearman's rank correlation coefficient or simple linear regression was used to describe the correlation between two variables. The number of animals and *p*-values are described in the figure legend or results text.

For details on CSD waveform sorting, histological assessment of infarct volume and cerebral blood flow and blood oxygenation analysis, see Supplementary Materials and Methods.

ACCEPTED MANUSCRIPT

Downloaded from academic.oup.com/brain/advance-article/doi/10.1093/brain/awag305/8788779 by guest on 24 November 2026

Results

Integrated multimodal platform enables simultaneous DC-coupled electrophysiology and CBF imaging

To investigate the relationship between CSDs, CBF, and tissue viability, we developed a multimodal platform combining DC-coupled graphene solution-gated field-effect transistor (gSGFET) arrays with LSCI (Fig. 1Ai). This setup enabled high-resolution mapping of both neuronal responses and rCBF in anesthetised mice undergoing focal cerebral ischaemia. A flexible gSGFET array, optically compatible with the wavelengths used in LSCI, was positioned epidurally over the cortex allowing for simultaneous electrophysiological recording and full-field optical imaging (Fig. S1Ai-ii). Prior to recordings, transistor-specific transfer curves were obtained to determine the optimal gate bias (Vgs) for maximizing current sensitivity (Ids)[20]. The DC-stable acquisition system preserved infraslow potentials crucial for resolving CSD waveforms (Fig. 1B). LSCI, focused through the gSGFET array, provided concurrent surface rCBF measurements with high spatiotemporal resolution (Fig. S1Bii).

Alternating current frequencies (AC-ECoG >0.5 Hz) were acquired alongside DC-coupled recordings and provided complementary information on spreading depression. AC activity was markedly suppressed following the onset of a CSD, consistent with spreading depression (Fig. S2A). Within the ischaemic core, this suppression was sustained with no evidence of recovery over the ~2 hr recording period (Fig. S2B). Channels located outside the core exhibited partial or complete recovery over time. Notably, channels close to the core (1.0–1.5 mm) showed more prolonged suppression compared to those further away (2.0–2.5 mm), indicating a spatial gradient in recovery. This gradient likely reflects regional variation in CSD duration. These patterns were observed in both focal cerebral ischaemia models.

CSD duration evolves with time following ischaemia

Focal cerebral ischaemia was induced using the PT model (Fig. 1Ai) and the dMCAo model (Fig. S3). Following PT, CSD duration increased over time when recorded from channels close to the ischaemic core (Fig. 2Ai and Bi). Analysis of channels within 1.0 – 1.5 mm of the core (Fig. 2Aii) showed that CSD duration increased from 51.0 ± 23.7 s at the start to 90.2 ± 37.0 s at the end of the experiment, representing a mean paired increase of 39.1 s (paired t-test, $p < 0.001$; $n = 18$) (Fig. 2Aiii). Channels further away from the core (2.0 – 2.5 mm) showed no change in duration with time (45.9 ± 18.7 s vs 46.6 ± 19.0 s; mean difference 0.7 s, paired t-test, p = NS; $n = 18$) (Fig 2. Aiv).

ACCEPTED MANUSCRIPT

Downloaded from academic.oup.com/brain/advance-article/doi/10.1093/brain/awag305/8788779 by guest on 24 November 2026

In the dMCAo model, a similar but more widespread increase in CSD duration was observed (Fig. 2Bi – ii). Channels within 1.0 – 1.5 mm of the ischaemic core showed an increase in duration from 111.6 ± 39.2 s at the start to 171.8 ± 48.0 s at the end of the experiment (mean paired increase 60.2 s, paired t-test, $p < 0.001$; $n = 16$) (Fig 2. Biii). Channels further from the core also exhibited a smaller but significant increase in CSD duration (62.5 ± 22.7 s vs 74.2 ± 24.8 s; mean difference 11.7 s, paired t-test, $p < 0.001$; $n = 14$) (Fig. 2Biv).

CSD duration is inversely correlated with regional perfusion following ischaemia

To determine how local tissue perfusion shapes CSD electrophysiology during ischaemia, a two-stage illumination protocol was applied, with 60 s of initial illumination followed by a further 180 s. The first illumination caused a minor, localised perfusion decrease (range 0.74 to 1.32, mean = 1.04; Fig. S7A) however no significant perfusion deficit developed (Fig. 1Aiii). A CSD was reliably induced, with a latency of 48.2 ± 20.9 s (Fig. 1Aii), from the area undergoing thrombosis, that would propagate underneath the array (Supplementary Video 1, available at FigShare: doi:10.6084/m9.figshare.33292710), with CSD duration showing no correlation with local perfusion (Fig. S8A). In contrast, a longer 180 s illumination produced a ~50% perfusion decrease near the illumination site (Fig. 1Aii and Fig. 3B) and a broad perfusion gradient formed beneath the recording array (Fig. S8B), resulting in frequent spontaneous CSDs ($n = 3.10 \pm 1.50$) over the 120 mins recording period. Under these conditions, localised clustering of CSDs could be observed (Fig. 3A and Supplementary Video 2, doi:10.6084/m9.figshare.33292710). Spatial origin of CSDs changed between the first and last CSDs in these models, with the first CSD detected close to the core and later CSDs recorded on more distal channels (Fig. S4A and B).

CSDs varied significantly in duration as they propagated across the array (range 15 to 190 s) and were strongly dependent on underlying rCBF (Fig. 3Bii & C). CSD duration negatively correlated with normalized perfusion (Fig. 3Di). Categorising CSDs by local perfusion revealed progressively shorter durations with increasing rCBF: 144.8 ± 26.8 s at 0.5 PU; 104.7 ± 39.4 s at 0.7 PU; 66.2 ± 33.9 s at 0.9 PU; and 51.5 ± 21.9 at 1.1 PU (One-way ANOVA, **** $p < 0.001$) (Fig. 3Dii).

Similar to the PT model, a perfusion gradient also formed beneath the gSGFET following dMCAo (Fig. S8C). An inverse correlation between CSD duration and perfusion was also observed in the dMCAo model (Fig. S9Bi-ii), where topical ferric chloride produced a rapid occlusion (Fig. S3) and CSD onset (CSD latency 215.5 ± 83.4 s, Fig. S9C). This together confirms that CSD duration reflects the underlying metabolic state across models. Figure 2Bi displays distinct electrophysiological responses that align with the perfusion gradient

ACCEPTED MANUSCRIPT

Downloaded from academic.oup.com/brain/advance-article/doi/10.1093/brain/awag305/8788779 by guest on 24 November 2026

and track the spatiotemporal evolution of propagating CSDs over the 90 mins recording period.

Distinct CSD waveform morphologies delineate perfusion-dependent tissue states

The spatial resolution of the gSGFET array allowed classification of CSD waveform morphologies within a single preparation (Fig. 4A). Across both stroke models, four distinct waveform types were identified: single peak (SP), double peak (DP), negative ultra-slow potential (NUP), and hyper-inverted (HI) (Fig. 4B). HI is a positive deflection observed in channels that previously recorded an NUP waveform, coinciding with the detection of DP or SP-type CSDs in adjacent gSGFETs. HI were only observed in depolarized tissue. The waveform types showed an association with local perfusion. In the PT model, SP CSDs were recorded at 0.96 ± 0.18 PU, DP at 0.70 ± 0.23 PU, NUP at 0.42 ± 0.18 PU, and HI at 0.48 ± 0.15 PU (One-way ANOVA, **** $p < 0.001$) (Fig. 4Ci-iii). DP waveforms were significantly longer in duration than SP (130.0 ± 59.0 s vs. 50.89 ± 21.92 s, **** $p < 0.001$) (Fig. 4Cii-Civ).

In the dMCAo model, similar trends were observed: SP at 0.80 ± 0.16 PU, DP at 0.65 ± 0.16 PU, NUP at 0.59 ± 0.12 PU, and HI at 0.51 ± 0.08 PU (Fig S10Ai & Aiii). DP waveforms again had significantly longer durations than SP (129.90 ± 58.97 s vs. 53.32 ± 20.47 s, unpaired t-test, **** $p < 0.001$) (Fig S10Aii & iv).

SP and DP CSD waveforms could be further classified based on the presence of hyperpolarisation at the onset, the termination, or at both phases (Fig S11A). Notably, SP CSDs with dual hyperpolarisation (DH) waveforms were significantly narrower than the other CSD waveform types (34.50 ±13.63; Fig S11Bi).

CSD-induced haemodynamic responses are predicted by local tissue state

To understand how CSDs influence local haemodynamics, we classified CSD-evoked rCBF changes into vasoconstrictive (VC), biphasic (BP), or vasodilatory (VD) responses (Fig. 5A). In the PT model, response types occurred at significantly different perfusion levels: VC at 0.79 ± 0.20 PU, BP at 0.85 ± 0.18 PU, and VD at 1.01 ± 0.18 PU (One-way ANOVA, **** $p < 0.001$) (Fig. 5Bi-ii), in accordance with literature about the vasoconstrictive response to CSD in poorly perfused tissue [12] (Supplementary Video 3, doi:10.6084/m9.figshare.33292710). CSD-induced vasodilatory responses were more frequently associated with SP waveforms, whereas DP, HI and NUP CSDs were predominantly linked to VC and BP haemodynamic responses (Fig. 5Biii) also supporting the relation between waveform type and perfusion obtained.

ACCEPTED MANUSCRIPT

Downloaded from academic.oup.com/brain/advance-article/doi/10.1093/brain/awag305/8788779 by guest on 24 November 2026

Occlusion of the dMCA also displayed all three CSD-induced haemodynamic patterns (Fig. S12A). CSD-evoked VC responses were recorded at 0.59 ± 0.17 PU, BP at 0.75 ± 0.18 PU, and VD at 0.74 ± 0.08 PU (One-way ANOVA, **** $p < 0.001$) (Fig. S11Bi-ii). Overall, these findings indicate that CSD-associated hemodynamic responses shift from vasodilation to vasoconstriction with increasing metabolic compromise.

DC-ECoG is a strong predictor of CSD-induced haemodynamics in focal cerebral ischaemia

CSDs were found to evoke distinct localised haemodynamic responses in acute focal cerebral ischaemia. To predict these response types (VD, BP, or VC) from DC-ECoG recordings, we developed a neural network model using only electrophysiological input features. Five progressively complex models were constructed by sequentially incorporating the following predictors: (1) DC-ECoG voltage traces, (2) first derivative, (3) second derivative, (4) CSD progression index (CPI), and (5) CSD duration (Fig. 5Ci–iii). The full model, integrating all five features, achieved a mean classification accuracy of 72% ± 9.27 ($p = 0.005$, bootstrap test). While this average accuracy reflects overall performance, it does not indicate class-specific discriminability. Receiver operating characteristic (ROC) analysis revealed that VD and BP were the most readily distinguishable, demonstrating a >70% classification accuracy using a single feature. In contrast, VC responses were more challenging to predict, but their classification improved substantially with the addition of higher order features. These findings demonstrate that distinct localised vascular responses to CSDs can be accurately inferred from DC-ECoG signals recorded with gSGFET arrays (Fig. 5Ciii).

Local haemodynamic and oxygenation changes associated with CSDs

Given the high metabolic demand imposed by CSDs, we monitored localized haemoglobin oxygenation levels to assess their contribution to disruptions in tissue oxygenation. We applied our multimodal recording setup to simultaneously monitor DC-ECoG, rCBF, and haemoglobin oxygenation dynamics (HbO and HbR; Fig. S13A) in a subset of animals (n=8). Focusing on CSD initiation, we observed that CSDs originating directly beneath the gSGFET array were preceded by a gradual decline in HbO commencing on average 79 s before CSD onset only in areas of

ACCEPTED MANUSCRIPT

Downloaded from academic.oup.com/brain/advance-article/doi/10.1093/brain/awag305/8788779 by guest on 24 November 2026

initiation [Fig. 6A(i and ii) and Supplementary Video 4 (doi:10.6084/m9.figshare.33292710)]. A decrease in rCBF in this region was not present preceding the CSD (Fig. 6Ai). In contrast, regions of CSD propagation displayed a significantly shorter pre-onset HbO decrease (8.1 s, unpaired t-test, **** $p < 0.001$) suggesting spatial specificity to pre-CSD metabolic shifts.

We next examined the temporal dynamics of HbO recovery relative to CSD repolarization. HbO restoration exhibited variability, occurring either before or after CSD recovery (Fig. 6Bi), potentially reflecting local impairments in neurovascular coupling. Notably, the latency of HbO recovery relative to CSD repolarization (with negative values indicating pre-repolarization recovery) correlated significantly with CSD duration (linear regression, $R^2 = 0.24$, $p < 0.001$; Fig. 56ii). To further characterise these dynamics, we quantified the full recovery time of both HbO and HbR following CSD onset (Fig. S13B). HbO recovery time was inversely correlated with normalised perfusion (PU), indicating that reduced perfusion significantly delays reoxygenation (Fig. S13Ci). In contrast, HbR recovery showed only a modest relationship with perfusion, suggesting differential regulation of oxygen delivery and extraction post-CSD (Fig. S13Cii).

CSD duration was significantly correlated with the recovery time of both HbO and HbR (Fig. S13Di-ii), indicating that prolonged depolarization imposes a sustained metabolic burden. Distinct CSD waveform morphologies were also predictive of oxygen dynamics. Specifically, NUP and DP waveforms were associated with extended HbO depletion (Fig. S13Ei). While HbR recovery was less tightly coupled to waveform features, NUP events exhibited significantly prolonged HbR recovery times relative to other waveform classes (Fig. S13Eii).

Ketamine shortens CSD duration and modulates waveform

To explore the effects of modulating CSD properties, we investigated the impact of ketamine (15 mg/kg IP) (Fig. 7A). We used a dose of ketamine that is reported as non-sedative in awake mice (Masvidal et al 2021). Following ketamine administration, CSD waveforms were shorter when compared to saline treated animals (Fig. 7B). Comparison of CSD durations recorded after the initial 60 s photothrombosis displayed no significant difference between groups (Fig S14A). However, after injecting ketamine and illuminating for 180 s, CSD duration no longer correlated significantly with perfusion (Spearman's $r = -0.14$, $p = 0.02$, $n = 7$), in contrast to the robust negative correlation observed in saline-treated animals (Spearman's $r = -0.65$, $p = 2.1e^{-25}$, $n = 15$) (Fig. 7Cii). CSD durations in ketamine-treated animals were significantly shorter at each perfusion level, notably durations reduced to 49.6 ± 43.7 s at 0.5 PU compared to 144.8 ± 26.8 s in saline controls

ACCEPTED MANUSCRIPT

Downloaded from academic.oup.com/brain/advance-article/doi/10.1093/brain/awag305/8788779 by guest on 24 November 2026

and 39.6 ± 24.2 at 0.7 PU compared to 104.7 ± 39.4 (two-way ANOVA, **** $p < 0.001$). SP waveform types were more common following ketamine administration displaying a reduction in longer DP CSDs (Fig. S14Bi-ii). The hyperpolarisation type of the SP CSD favoured the DH waveform which exhibited the shortest duration (24.34 ± 9.64; Fig. S11Bii). The number of spontaneous CSDs did not change between groups following 180 s illumination (Fig S14Ci). CSD propagation speed in ketamine animals was comparable to saline controls for the first and second CSDs but then began to significantly differ with subsequent CSDs (Fig S14Cii).

Ketamine prevents CSD-induced inverse haemodynamic responses

In saline-treated animals, CSDs in metabolically compromised regions predominantly evoked vasoconstriction (Fig. 8A). Administration of ketamine markedly attenuated these vasoconstrictive responses. Of the 366 responses recorded in ketamine treated animals, 343 were VD and 23 BP. In contrast, saline treated animals exhibited a broader distribution (432 responses), of which 71 were VD, 154 BP and 207 VC. There is a significant mean increase in vasodilation responses in the ketamine treated animals (53.5 ± 38.4) when compared to saline treated animals (8.1±8.4) (Fig. 8Bi). Representative traces confirmed the conversion of vasoconstrictive to vasodilatory responses even in low-perfusion regions, suggesting that ketamine suppresses the pathological inverse haemodynamic response to CSD. Resting rCBF, assessed 1.5 h after the 180 s illumination, was significantly elevated in ketamine-treated animals relative to the distance from the lesion core (Fig. 8C). While normalised perfusion declined following multiple CSDs in saline-treated animals (Fig. S15Ai), ketamine treatment led to a sustained increase in perfusion across successive CSDs (Fig. S15Aii). Notably, groupwise analysis of the 3rd CSD revealed significantly enhanced perfusion at 1.5 and 2.0 mm from the lesion in the ketamine cohort (Fig. 8D). In this model, administration of ketamine 5 s prior to the 2nd illumination resulted in a significant reduction in infarct volume compared with saline injected animals. Mean lesion volumes were 14.5 ± 1.8 mm^3 ($n = 5$) in the saline group and 7.1 ± 2.0 mm^3 ($n = 6$) in the ketamine group (unpaired t-test, **** $p < 0.001$; Fig. 8Ei-ii). Collectively, these findings underscore the capacity of our gSGFET-LSCI platform to resolve dynamic neurovascular responses with high spatiotemporal fidelity and identify ketamine as a potent modulator of CSD-induced haemodynamics in the ischaemic brain.

ACCEPTED MANUSCRIPT

Downloaded from academic.oup.com/brain/advance-article/doi/10.1093/brain/awag305/8788779 by guest on 24 November 2026

Discussion

Our study establishes a multimodal platform that integrates flexible graphene-based micro-transistor arrays with LSCI to resolve CSDs and their associated vascular responses with high spatiotemporal fidelity. Achieving sufficient spatial resolution to map CSD waveforms and their impact on perfusion within complex ischaemic regions has remained challenging with conventional electrophysiological approaches. Aside from approaches such as wide-field calcium imaging [38], existing tools lack the spatial resolution and stability required to map these processes in vivo. Our approach overcomes long standing technical limitations in studying CSD dynamics and their impact on secondary injury in stroke.

Using the described multimodal approach, we tracked the evolution of ischaemia in specific cortical regions over relatively short time periods (Fig. 2Ai and Bi). CSD waveforms shifted with declining perfusion from short duration monophasic events to biphasic and prolonged forms, and ultimately to NUPs and HI patterns, providing a dynamic electrophysiological marker of lesion progression and evolving tissue metabolic state. We show that CSD waveform features, particularly duration and waveform complexity, scale with regional perfusion and thus reflect local tissue health. In metabolically intact cortex, CSDs remain coupled to vasodilation, whereas ischaemic regions exhibit prolonged, complex waveforms with biphasic peaks and frequently localised vasoconstriction. These distinct electrophysiological phenotypes therefore index the tissue's metabolic capacity, delineate a continuum of tissue states, and predict the ensuing haemodynamic response, supporting the hypothesis that CSD duration [39] and, as shown in this study, CSD waveform shape serve as a real-time biomarker of regional tissue health.

The HI CSD waveform, detected within the ischaemic core, represents a previously undescribed electrographic marker for delineating core tissue. In our acute experiments, the HI CSD waveform would occur after the same channel had previously recorded an NUP. Although definitive interpretation will require future laminar depth recordings, we propose that HI waveforms arise when subsequent CSDs propagate at the boundary between persistently depolarised core tissue and surrounding viable cortex, producing a dipole-like surface signal rather than a conventional superficial DC shift. If confirmed, the HI waveform could allow the electrographic localisation of the ischaemic core hours after the insult in rodents or humans – even without the initial NUP recording. Channels recording outside the ischaemic core would record SP or DP CSDs whereas channels inside the core would record HI.

The multichannel nature of gSGFET arrays enabled the reliable detection of a CSD that initiated directly beneath it. In such cases, we observe a highly localised pre-CSD decrease in HbO at the site of initiation, underscoring the spatial resolution of our platform. Notably,

ACCEPTED MANUSCRIPT

Downloaded from academic.oup.com/brain/advance-article/doi/10.1093/brain/awag305/8788779 by guest on 24 November 2026

we identify a gradual HbO decrease >60 s before CSD onset. Although reductions in tissue oxygenation and HbO preceding CSDs are well described in experimental and clinical ischaemia[13,39–41], our data highlights a spatially localized and progressive HbO decline immediately preceding CSD initiation directly underneath the recording array, enabling co-registration with DC-coupled CSD waveform dynamics and local perfusion gradients.

This observation provides mechanistic insight into how CSDs are initiated in ischaemic tissue. A localised supply demand imbalance, driven by heightened metabolic activity, develops before depolarization onset. Such a mismatch may create the permissive conditions that lower the threshold for CSD initiation. CSD induced changes in blood oxygenation have been observed clinically, with a study reporting that the absence of a change in blood oxygenation response to CSD correlated with poor outcomes in patients with malignant stroke [40]. While we did not observe this association, this probably reflects the earlier timepoint of our measurements and the comparatively less severe pathology in our rodent models.

In addition to experimental mapping, we implemented a neuronal mass model using a convolutional neural network trained on DC-ECoG parameters to predict haemodynamic responses. By capturing the nonlinear, multivariate relationships between waveform features and vascular outcome, this approach was well suited to the dataset and successfully classified three distinct haemodynamic responses with ~70% accuracy. These results indicate that a substantial proportion of haemodynamic variance is captured by features of the DC-coupled electrophysiological waveform in our experimental conditions. This raises the possibility that regional vascular responses to CSDs could, in principle, be inferred from DC-coupled electrophysiology alone in settings where direct blood flow monitoring is not feasible, providing a potential route toward simplified neuromonitoring strategies. However, because the relationship between CSD waveform dynamics and associated haemodynamic responses may be modified by pharmacological interventions and other pathophysiological variables, particularly in the clinically heterogeneous setting, this approach will require prospective validation under clinically relevant conditions. Although the present accuracy is limited by dataset size, it is likely to improve with larger training sets and incorporation of additional physiological variables, ultimately advancing toward real-time inference of tissue perfusion and vascular response in both experimental and clinical neuromonitoring contexts.

There is evidence to support ketamine as a cerebral vasodilator [41–44], and our findings reveal a mechanistic basis for its neuroprotective potential in ischaemic stroke. We show that the CSD-induced haemodynamic response is dictated by local perfusion: poorly perfused

ACCEPTED MANUSCRIPT

Downloaded from academic.oup.com/brain/advance-article/doi/10.1093/brain/awag305/8788779 by guest on 24 November 2026

tissue typically exhibits long duration CSDs and vasoconstriction, whereas adequately perfused regions show shorter duration CSDs and vasodilation. Systemic administration of a low, non-sedative dose of ketamine not only improved cortical perfusion surrounding the ischaemic core but also shortened CSD duration. However, ketamine did not alter CSD frequency compared with saline treated mice (Fig S14Ci). This contrasts with studies using higher ketamine doses that suppress CSD occurrence[30–33], suggesting that low-dose ketamine preferentially modifies CSD dynamics and neurovascular coupling rather than preventing CSD initiation. Ketamine altered the CSD-induced haemodynamic response, shifting it from a predominantly biphasic response to a vasodilatory profile, even within regions that remained underperfused. In severely hypoperfused cortex, where CSDs in vehicle treated animals consistently evoked vasoconstriction, ketamine abolished these inverse responses and, in some cases, promoted vasodilation. By preventing this inverse haemodynamic response, ketamine preserves vasodilatory coupling to CSD across compromised cortex, thereby interrupting the pathological cycle of spreading ischaemia, energy failure, and recurrent CSDs. Spatially resolved HbO imaging was not available for the ketamine experiments, and future work will be required to determine whether ketamine-induced vascular modulation translates into improved tissue oxygenation and metabolic benefit.

Ketamine was evaluated in the photothrombotic model because its reproducible lesion formation, reliable CSD occurrence, and well-defined perfusion gradients provide a controlled platform for assessing pharmacological modulation of CSD waveform and haemodynamic responses. Importantly, both stroke models exhibited the same relationship between local perfusion and CSD waveform phenotype, suggesting that the underlying mechanism by which ketamine modulates CSDs may generalise across experimental models of focal cerebral ischaemia. Future studies should evaluate these findings in additional preclinical stroke models.

This study provides a direct explanation for ketamine's neuroprotective action in acute brain injury and is consistent with prior preclinical and clinical reports of its efficacy in suppressing CSDs and limiting lesion expansion [25–28,32–35,45]. Although ketamine has a relatively short half-life[21], most CSDs in our models occurred during the early post-ischaemic period immediately following lesion induction. Transient shortening of metabolically demanding CSDs, coupled with an inhibition of the CSD induced haemodynamic response and the promotion of vasodilation, is therefore expected to reduce lesion expansion. Consistent with this, we show a decrease in lesion volume in ketamine treated animals in this model. Together, these findings highlight the translational relevance of our platform for identifying drug effects on neurovascular dynamics and

ACCEPTED MANUSCRIPT

Downloaded from academic.oup.com/brain/advance-article/doi/10.1093/brain/awag305/8788779 by guest on 24 November 2026

support ketamine's potential as a therapeutic modulator of spreading depolarizations in stroke.

Our findings suggest that real time monitoring of high-fidelity DC-couple electrophysiological data could provide functional biomarkers of tissue viability. By improving the detection and characterisation of spreading depolarizations, this approach may support dynamic assessment of injury progression and allow for the stratification of patient populations most likely to benefit from targeted neuroprotective interventions [22,46]. Enhanced CSD monitoring may also benefit other neurological disorders, including traumatic brain injury, subarachnoid haemorrhage, and epilepsy in which CSD events similarly mark evolving metabolic stress and therapeutic opportunity.

A limitation of this work is that all experiments were performed in mice. Although mice are well suited for mechanistic studies of CSD, CSD-associated haemodynamic responses vary across species, and mice in particular show a greater propensity for vasoconstrictive components than larger mammals and humans [47]. However, vasoconstrictive CSD responses are also considered among the most clinically pathological in humans, and our finding that ketamine prevents CSD-induced vasoconstriction therefore remains directly relevant despite potential interspecies differences in the overall neurovascular profile.

In summary, our findings define distinct electrophysiological signatures of CSDs that encode tissue state and vascular response in ischaemic stroke. By leveraging high-resolution, multimodal recordings, we identify ketamine as a potent modulator of CSD waveform dynamics and cerebrovascular outcome, advancing the framework for therapeutic intervention in acute brain injury. Although demonstrated here in ischaemia, perfusion-linked CSD signatures may extend to other conditions where spreading depolarizations drive pathology, including traumatic brain injury and subarachnoid haemorrhage.

Future studies should explore how CSD waveform phenotypes evolve in the subacute phases of stroke. Additionally, integrating this platform with calcium imaging [48], optogenetics [21,49–51] or metabolic biosensors could deepen our understanding of the cellular mechanisms that govern CSD initiation, propagation, and resolution, as well as their regional impact on tissue health under pathological conditions.

Data availability

All relevant data obtained to evaluate the main findings of the paper are openly available from the corresponding author upon reasonable request.

ACCEPTED MANUSCRIPT

Downloaded from academic.oup.com/brain/advance-article/doi/10.1093/brain/awag305/8788779 by guest on 24 November 2026

Acknowledgements

The thumbnail image for the online table of contents was partially created in BioRender. Flaherty, S. (2026) https://BioRender.com/pi4v05c.

Funding

This research was funded by the European Union's Horizon 2020 research and innovation programme under grant agreement no. 881603 (Graphene Flagship Core 3) and the European Union's Horizon Europe research and innovation programme under grant agreement 101130650 (META-BRAIN). This work was supported by the Medical Research Council [Grant Ref: MR/Y014545/1]. IMB-CNM is supported by the María de Maeztu Units of Excellence programme (Grant CEX2023-001397-M), funded by MCIN and MCIU/AEI/10.13039.501100011033. This research was supported by the Spanish Ministerio de Ciencia e Innovación through grant PID2021-126117NA-I00 funded by MCIU/AEI/10.13039/ 501100011033) and by "ERDF A way of making Europe", and grants PLEC2022-009232 & CNS2023-144492 funded by MCIU/AEI /10.13039/501100011033 and the European Union Next-GenerationEU/PRTR. This work has made use of the Spanish ICTS Network MICRONANOFABS, partially supported by MICINN and the ICTS NANBIOSIS, specifically by the Micro-NanoTechnology Unit U8 of the CIBER-BBN. This research was supported by CIBER -Consorcio Centro de Investigación Biomédica en Red- (CB06/01/0049), Instituto de Salud Carlos III, Ministerio de Ciencia e Innovación. Dr. Wykes was supported by a Senior Fellowship from the Worshipful Company of Pewterers.

Competing interests

J.M, C.J, and R.M are employees of Multichannel Systems, which is developing/commercialising the graphene-based technology described in this manuscript. J.A.G, K.K and A.G.-B declare financial interest in INBRAIN Neuroelectronics. All other authors declare no competing interests.

ACCEPTED MANUSCRIPT

Downloaded from academic.oup.com/brain/advance-article/doi/10.1093/brain/awag305/8788779 by guest on 24 November 2026

Supplementary material

Supplementary material is available at *Brain* online.

References

1. Leao, A. A. P. Spreading depression of activity in the cerebral cortex. *Journal of Neurophysiology* **7**, 359–390 (1944).
2. Dreier, J. P. The role of spreading depression, spreading depolarization and spreading ischemia in neurological disease. *Nat Med* **17**, 439–447 (2011).
3. Hartings, J. A. *et al.* The continuum of spreading depolarizations in acute cortical lesion development: Examining Leão's legacy. *J Cereb Blood Flow Metab* **37**, 1571–1594 (2017).
4. Hansen, A. J. & Zeuthen, T. Extracellular ion concentrations during spreading depression and ischemia in the rat brain cortex. *Acta Physiol Scand* **113**, 437–445 (1981).
5. Takano, T. *et al.* Cortical spreading depression causes and coincides with tissue hypoxia. *Nat Neurosci* **10**, 754–762 (2007).
6. Andrew, R. D. *et al.* The Critical Role of Spreading Depolarizations in Early Brain Injury: Consensus and Contention. *Neurocrit Care* **37**, 83–101 (2022).
7. Mies, G., Iijima, T. & Hossmann, K. A. Correlation between peri-infarct DC shifts and ischaemic neuronal damage in rat. *Neuroreport* **4**, 709–711 (1993).
8. Dijkhuizen, R. M. *et al.* Correlation between tissue depolarizations and damage in focal ischemic rat brain. *Brain Res* **840**, 194–205 (1999).
9. Hartings, J. A., Rolli, M. L., Lu, X.-C. M. & Tortella, F. C. Delayed secondary phase of peri-infarct depolarizations after focal cerebral ischemia: relation to infarct growth and neuroprotection. *J Neurosci* **23**, 11602–11610 (2003).
10. Dreier, J. P. *et al.* Ischemia caused by inverse coupling between neuronal activation and cerebral blood flow in rats. *International Congress Series* **1235**, 487–492 (2002).

ACCEPTED MANUSCRIPT

Downloaded from academic.oup.com/brain/advance-article/doi/10.1093/brain/awag305/8788779 by guest on 24 November 2026

11. Sukhotinsky, I., Dilekoz, E., Moskowitz, M. A. & Ayata, C. Hypoxia and Hypotension Transform the Blood Flow Response to Cortical Spreading Depression from Hyperemia into Hypoperfusion in the Rat. *J Cereb Blood Flow Metab* **28**, 1369–1376 (2008).

12. Ayata, C. & Lauritzen, M. Spreading Depression, Spreading Depolarizations, and the Cerebral Vasculature. *Physiol Rev* **95**, 953–993 (2015).

13. Dreier, J. P., Lemale, C. L., Kola, V., Friedman, A. & Schoknecht, K. Spreading depolarization is not an epiphenomenon but the principal mechanism of the cytotoxic edema in various gray matter structures of the brain during stroke. *Neuropharmacology* **134**, 189–207 (2018).

14. Dreier, J. P. *et al.* Ischaemia triggered by spreading neuronal activation is inhibited by vasodilators in rats. *The Journal of Physiology* **531**, 515–526 (2001).

15. Shin, H. K. *et al.* Vasoconstrictive neurovascular coupling during focal ischemic depolarizations. *J Cereb Blood Flow Metab* **26**, 1018–1030 (2006).

16. Nitric Oxide Scavenging by Hemoglobin or Nitric Oxide Synthase Inhibition by N-Nitro-L-Arginine Induces Cortical Spreading Ischemia When K+ Is Increased in the Subarachnoid Space - Jens P. Dreier, Katrin Körner, Nathalie Ebert, Astrid Görner, Inger Rubin, Tobias Back, Ute Lindauer, Tilo Wolf, Arno Villringer, Karl Max Einhäupl, Martin Lauritzen, Ulrich Dirnagl, 1998. https://journals.sagepub.com/doi/10.1097/00004647-199809000-00007?url_ver=Z39.88-2003&rfr_id=ori:rid:crossref.org&rfr_dat=cr_pub%20%200pubmed.

17. Li, C. *et al.* Evaluation of microelectrode materials for direct-current electrocorticography. *J. Neural Eng.* **13**, 016008 (2015).

18. Fabricius, M. *et al.* Association of seizures with cortical spreading depression and peri-infarct depolarisations in the acutely injured human brain. *Clin Neurophysiol* **119**, 1973–1984 (2008).

19. Nelson, M. J., Pouget, P., Nilsen, E. A., Patten, C. D. & Schall, J. D. Review of signal distortion through metal microelectrode recording circuits and filters. *J Neurosci Methods* **169**, 141–157 (2008).

20. Masvidal-Codina, E. *et al.* High-resolution mapping of infraslow cortical brain activity enabled by graphene microtransistors. *Nature Mater* **18**, 280–288 (2019).

ACCEPTED MANUSCRIPT

Downloaded from academic.oup.com/brain/advance-article/doi/10.1093/brain/awag305/8788779 by guest on 24 November 2026

21. Masvidal-Codina, E. *et al.* Characterization of optogenetically-induced cortical spreading depression in awake mice using graphene micro-transistor arrays. *J Neural Eng* **18**, (2021).

22. Wykes, R. C., Masvidal-Codina, E., Guimerà-Brunet, A. & Garrido, J. A. The advantages of mapping slow brain potentials using DC-coupled graphene micro-transistors: Clinical and translational applications. *Clin Transl Med* **12**, e968 (2022).

23. Watson, B. D., Dietrich, W. D., Busto, R., Wachtel, M. S. & Ginsberg, M. D. Induction of reproducible brain infarction by photochemically initiated thrombosis. *Ann Neurol* **17**, 497–504 (1985).

24. Karatas, H. *et al.* Thrombotic distal middle cerebral artery occlusion produced by topical FeCl3 application: a novel model suitable for intravital microscopy and thrombolysis studies. *J Cereb Blood Flow Metab* **31**, 1452–1460 (2011).

25. Reinhart, K. M., Morton, R. A., Brennan, K. C., Carlson, A. P. & Shuttleworth, C. W. Ketamine improves neuronal recovery following spreading depolarization in peri-infarct tissues. *J Neurochem* **168**, 855–867 (2024).

26. Hernández-Cáceres, J., Macias-González, R., Brožek, G. & Bureš, J. Systemic ketamine blocks cortical spreading depression but does not delay the onset of terminal anoxic depolarization in rats. *Brain Research* **437**, 360–364 (1987).

27. Pacheco, J. M. *et al.* Spreading Depolarizations Occur in Mild Traumatic Brain Injuries and Are Associated with Postinjury Behavior. *eNeuro* **6**, ENEURO.0070-19.2019 (2019).

28. Sánchez-Porras, R. *et al.* Ketamine modulation of the haemodynamic response to spreading depolarization in the gyrencephalic swine brain. *J Cereb Blood Flow Metab* **37**, 1720–1734 (2017).

29. Zheng, Z. *et al.* Spreading Depolarization during the Acute Stage of Experimental Subarachnoid Hemorrhage in Mice. *Acta Neurochir Suppl* **127**, 97–103 (2020).

30. Sánchez-Porras, R. *et al.* Eighteen-hour inhibitory effect of s-ketamine on potassium- and ischemia-induced spreading depolarizations in the gyrencephalic swine brain. *Neuropharmacology* **216**, 109176 (2022).

ACCEPTED MANUSCRIPT

Downloaded from academic.oup.com/brain/advance-article/doi/10.1093/brain/awag305/8788779 by guest on 24 November 2026

31. Sánchez-Porras, R. *et al.* The effect of ketamine on optical and electrical characteristics of spreading depolarizations in gyrencephalic swine cortex. *Neuropharmacology* **84**, 52–61 (2014).

32. Carlson, A. P., Abbas, M., Alunday, R. L., Qeadan, F. & Shuttleworth, C. W. Spreading depolarization in acute brain injury inhibited by ketamine: a prospective, randomized, multiple crossover trial. *J Neurosurg* **130**, 1513–1519 (2019).

33. Hertle, D. N. *et al.* Effect of analgesics and sedatives on the occurrence of spreading depolarizations accompanying acute brain injury. *Brain* **135**, 2390–2398 (2012).

34. Santos, E. *et al.* Lasting s-ketamine block of spreading depolarizations in subarachnoid hemorrhage: a retrospective cohort study. *Crit Care* **23**, 427 (2019).

35. Sakowitz, O. W. *et al.* Preliminary evidence that ketamine inhibits spreading depolarizations in acute human brain injury. *Stroke* **40**, e519-522 (2009).

36. Schaefer, N. *et al.* Multiplexed neural sensor array of graphene solution-gated field-effect transistors. *2D Mater.* **7**, 025046 (2020).

37. Ismail Fawaz, H., Forestier, G., Weber, J., Idoumghar, L. & Muller, P.-A. Deep learning for time series classification: a review. *Data Min Knowl Disc* **33**, 917–963 (2019).

38. Zhao, H. T. *et al.* Neurovascular dynamics of repeated cortical spreading depolarizations after acute brain injury. *Cell Reports* **37**, 109794 (2021).

39. Lauritzen, M. *et al.* Clinical Relevance of Cortical Spreading Depression in Neurological Disorders: Migraine, Malignant Stroke, Subarachnoid and Intracranial Hemorrhage, and Traumatic Brain Injury. *J Cereb Blood Flow Metab* **31**, 17–35 (2011).

40. Hecht, N. *et al.* Reduced brain oxygen response to spreading depolarization predicts worse outcome in ischaemic stroke. *Brain* awae376 (2024) doi:10.1093/brain/awae376.

41. Oren, R. E., Rasool, N. A. & Rubinstein, E. H. Effect of ketamine on cerebral cortical blood flow and metabolism in rabbits. *Stroke* **18**, 441–444 (1987).

42. Zeiler, F. A. *et al.* The Cerebrovascular Response to Ketamine: A Systematic Review of the Animal and Human Literature. *Journal of Neurosurgical Anesthesiology* **28**, 123 (2016).

ACCEPTED MANUSCRIPT

Downloaded from academic.oup.com/brain/advance-article/doi/10.1093/brain/awag305/8788779 by guest on 24 November 2026

43. Lei, H. *et al.* The effects of ketamine-xylazine anesthesia on cerebral blood flow and oxygenation observed using nuclear magnetic resonance perfusion imaging and electron paramagnetic resonance oximetry. *Brain Res* **913**, 174–179 (2001).

44. Cavazzuti, M., Porro, C. A., Biral, G. P., Benassi, C. & Barbieri, G. C. Ketamine Effects on Local Cerebral Blood Flow and Metabolism in the Rat. *J Cereb Blood Flow Metab* **7**, 806–811 (1987).

45. Takano, T. *et al.* Cortical spreading depression causes and coincides with tissue hypoxia. *Nat Neurosci* **10**, 754–762 (2007).

46. Hartings, J. A. *et al.* Improving Neurotrauma by Depolarization Inhibition With Combination Therapy: A Phase 2 Randomized Feasibility Trial. *Neurosurgery* **93**, 924–931 (2023).

47. Dreier, J. P. *et al.* All Three Supersystems—Nervous, Vascular, and Immune—Contribute to the Cortical Infarcts After Subarachnoid Hemorrhage. *Transl. Stroke Res.* **16**, 96–118 (2025).

48. Balbi, M. *et al.* Targeted ischemic stroke induction and mesoscopic imaging assessment of blood flow and ischemic depolarization in awake mice. *Neurophotonics* **4**, 035001 (2017).

49. Rossi, L. F., Wykes, R. C., Kullmann, D. M. & Carandini, M. Focal cortical seizures start as standing waves and propagate respecting homotopic connectivity. *Nat Commun* **8**, 217 (2017).

50. Rossi, L. F., Kullmann, D. M. & Wykes, R. C. The Enlightened Brain: Novel Imaging Methods Focus on Epileptic Networks at Multiple Scales. *Front Cell Neurosci* **12**, 82 (2018).

51. Sugimoto, K. *et al.* Optogenetic Spreading Depolarizations Do Not Worsen Acute Ischemic Stroke Outcome. *Stroke* **54**, 1110–1119 (2023).

Figure legends

Figure 1 Experimental paradigm and recording configuration. (**Ai)** Schematic of the experimental timeline for acute photothrombotic induction of focal cerebral ischaemia in anaesthetised mice. The setup enabled simultaneous DC-coupled electrophysiological recordings and laser speckle contrast imaging (LSCI) at the cortical surface beneath the transparent gSGFET array. Representative LSCI images display cortical blood flow (CBF) at baseline (pre-illumination), following a 60 s illumination (evoking a control CSD with minimal ischaemic insult) and after 180 s illumination (significant ischaemic insult).

ACCEPTED MANUSCRIPT

Downloaded from academic.oup.com/brain/advance-article/doi/10.1093/brain/awag305/8788779 by guest on 24 November 2026

Animals were culled at timepoint 3 hrs after recording sessions. (**Aii**) Bar graph of CSD latency (s) following photothrombosis (n = 18). (**Aiii**) Bar graphs displaying normalised perfusion (PU) plotted against distance to lesion (mm) following an initial 60 s (369 ROIs; n = 15) and an extended 180 s (944 ROIs; n = 15) illumination (mean ± s.d.), respectively. (**B**) Spatial map of DC-ECoG (<1 Hz) traces from 29 of 30 functional transistors arranged in a 5 x 6 grid configuration, demonstrating the spatial resolution of the 2.9 x 2.4 mm gSGFET array following the second (180 s) illumination. Figure partially created in BioRender. Flaherty, S. (2026) https://

BioRender.com/5u3ywuu.

Figure 2 CSD duration evolution with time. (**Ai**) Representative 90 min DC-coupled (DC-ECoG < 0.1 Hz) gSGFET recording following PT in anaesthetised mice. Channels have been selected at increasing distances from the lesion core, with 0.5 mm spacing. Channel positions are shown on the gSGFET array map together with the ischaemia location (green laser) (**Aii**) Zoom in on the 3rd and 4th CSD from channel E22 (in Ai) which occur 35 mins apart. (**Aiii)** A comparison of the start and end CSD duration 1.0 -1.5 mm away from the ischaemic core post PT induction. Each paired data point is a single channel (paired t-test, **** $p < 0.001$, n = 18) (**Aiv**) A comparison of the start and end CSD duration 2.0 - 2.5 mm away from the ischaemic core. Each paired data point is a single channel (paired t-test, p = ns, n = 18). (**Bi**) Example 110 min DC-coupled (DC-ECoG < 0.1 Hz) gSGFET recording following dMCAo in anaesthetised mice. Channels have been selected at increasing distances from the lesion core, with 0.5 mm spacing. Channel positions are shown on the gSGFET array map together with the ischaemia location (dMCA bifurcation) (**Bii**) Zoom in on the 2nd and 3rd CSD from channel E14 (in Bi) which occur 80 mins apart. (**Biii**) A comparison of the first and last CSD duration 1.0 -1.5 mm away from the ischaemic core following post dMCAo induction. Each paired data point is a single channel (paired t-test, **** $p < 0.001$, n = 14). (**Biv**) A comparison of the first and last CSD duration 2.0 - 2.5 mm away from the ischaemic core. Each paired data point is a single channel (paired t-test, **** $p < 0.001$, n = 14). Figure partially created in BioRender. Flaherty, S. (2026) https://BioRender.com/hxthhf4.

Figure 3 Duration of ischaemia-induced cortical spreading depolarizations (CSDs) is dependent on regional cerebral blood flow (rCBF). (**A**) An example 30 min DC-ECoG (< 0.1 Hz) recording acquired using a gSGFET array following 180 s photothrombotic induction of focal cerebral ischaemia (green laser) in anaesthetised mice. 28 of 30 active transistors

ACCEPTED MANUSCRIPT

Downloaded from academic.oup.com/brain/advance-article/doi/10.1093/brain/awag305/8788779 by guest on 24 November 2026

illustrate the spatial and temporal mapping of CSD propagation across the cortical surface (**Bi**) Single frame laser speckle contrast imaging (LSCI) showing resulting perfusion deficit (dark blue region) following 180 s photothrombosis. The recording gSGFET is highlighted by a white box. (**Bii**) Heatmap of CSD duration (s) for a single CSD event recorded in the same preparation as Bi. Empty boxes indicate non-functioning channels; the red outline marks the channel nearest the lesion core. (**Ci**) Representative CSD traces recorded in regions with differing normalised perfusions (PU), illustrating perfusion-dependant CSD duration. The dotted redline indicates the change in CSD duration. (**Cii)**. Overlay of 29 CSD traces from a single CSD event recorded across a 30 channel gSGFET array. Trace colour represents CSD duration (s). (**Di**) Scatter plot displaying a significant negative correlation between CSD duration (s) and underlying normalised perfusion (PU) (161 CSDs, Spearman's r = -0.65, p = 2.1e^{-25}; n = 15). (**Dii**) Grouped analysis of mean CSD duration (s) as a function of normalised perfusion (PU) (161 CSDs; n =15), revealing significant differences across most perfusion bins (mean ± s.d.). Figure partially created in BioRender. Flaherty, S. (2026) https://BioRender.com/fhi5n2e.

Figure 4 Cortical spreading depolarization waveforms are dependent on regional cerebral blood flow (rCBF). (**A)** Four distinct CSD waveform types were identified: Negative ultra-slow potential (NUP), double peak (DP), single peak (SP) and hyper inverted (HI). (**B**) Representative CSD waveform types recorded across 29 out of 30 functional gSGFET channels in response to photothrombotic induction of focal cerebral ischaemia. (**Ci**) Plot displaying CSD waveform types (457 SP, 113 DP, 22 NUP and 39 HI waveforms; n = 15) as a function of mean normalised perfusion (PU) demonstrating perfusion-dependant waveform types (**Cii**) Comparison of mean SP and DP CSD (535 SP and 192 DP CSDs; n = 15) duration (s) highlighting prolonged durations associated with DP CSDs. (**Ciii)** Density plots showing the distribution of CSD waveform types across a range of normalised perfusions (PU). (**Civ**) Density plot of SP and DP CSD duration (s) distribution. Figure partially created in BioRender. Flaherty, S. (2026) https://BioRender.com/o9d0ac3.

Figure 5 Cortical spreading depolarization induced haemodynamics. (**A**) Example DC-ECoG and rCBF traces post photothrombosis in anaesthetised mice with labelled CSD induced haemodynamic response. Three haemodynamic responses were observed in this work, vasoconstriction (VC), biphasic response (BP) and vasodilation. (**Bi-ii**) CSD-induced haemodynamic response type plotted in function of mean normalised perfusion (PU) and presented as a density distribution plot (361 ROIs; n = 15). (**Ci**) Average neural network model accuracy as a function of the incremental addition of DC-ECoG derived predictors

ACCEPTED MANUSCRIPT

Downloaded from academic.oup.com/brain/advance-article/doi/10.1093/brain/awag305/8788779 by guest on 24 November 2026

(DC-ECoG, DC-ECoG 1st derivative, DC-ECoG 2nd derivative, CSD progression index (CPI) and CSD duration). (**Cii**) Class specific accuracy as a function of model complexity. (**Ciii**) Receiver Operating Characteristic (ROC) curves showing the model's ability to correctly identify each type of CSD induced vascular response based on recorded DC-ECoG activity. Black dotted line reflects guessing; lines above or below the black line indicate that performance is better or worse than guessing, respectively. Area under ROC curve corresponds to classification accuracy. Figure partially created in BioRender. Flaherty, S. (2026) https://BioRender.com/7u86zr9.

Figure 6 Oxygenated haemoglobin (OxyHb) and cortical spreading depolarization dynamics following focal cerebral ischaemia. (**Ai-ii**) Example DC-ECoG (black traces <0.1 Hz), OxyHb (green traces) and normalised perfusion (purple traces) traces displaying a gradual OxyHb decrease preceding CSD initiation underneath the recording gSGFET array. In areas of CSD propagation, there is minimal pre-CSD OxyHb decrease (22 ROIs; $n = 6$). (**Bi**) Example traces displaying OxyHb (green traces) recovery pre, in sync with or post CSD repolarization (DC-ECoG < 0.1 Hz black traces). Blue dotted lines mark recovery of DC-ECoG and OxyHb. (**Bii**) Line plot of CSD duration (s) and OxyHb recovery (s) (87 CSDs, linear regression, R squared = 0.24, $p < 0.001$; $n = 7$). Pre CSD repolarsation OxyHb recovery by a negative value and post CSD repolarization OxyHb recovery is indicated by a positive value. Figure partially created in BioRender. Flaherty, S. (2026) https://BioRender.com/f954up4.

Figure 7 Ketamine modulation of cortical spreading depolarization (CSD) duration and waveform. (**Ai**) Three examples DC-ECoG traces displaying a 100 mins recording and annotated with experimental protocol. 1st 60 s and 2nd 180 s photothrombosis are marked by green arrows. Saline or 15mg/kg ketamine was administered via IP injection moments after the 2nd illumination (black arrow) (**Aii**) Single frame from Laser speckle contrast imaging (LSCI) characterising an area of cerebral ischaemia following photothrombosis (dark blue region) and 3 highlighted gSGFETs at 0.5 mm separation. The selected channel recordings from this experiment are plotted in Ai. (**Aiii**) CSD duration (s) displayed as a 5x6 heatmap. Each trace is 250 s in length. (**B**) Four overlaid CSD traces from saline- and ketamine-treated animals, recorded within tissue exhibiting comparable normalised perfusion levels (0.7 – 0.8 PU). Note the reduction in CSD duration (s) (**Ci**). Comparison of the correlation between CSD duration (s) and normalised perfusion (PU) between saline injected animals (161 CSDs, r = -0.65, $p = 2.1e^{-25}$; $n = 15$) and ketamine injected animals (269 CSDs, $r = -0.14$, $p = 0.02$; $n = 7$) post photothrombosis. (**Cii**). Plot of CSD duration (s),

ACCEPTED MANUSCRIPT

Downloaded from academic.oup.com/brain/advance-article/doi/10.1093/brain/awag305/8788779 by guest on 24 November 2026

from saline and ketamine injected animals in function of normalised perfusion (PU). (saline group 161 CSDs, *n* =15 and ketamine group 269 CSDs, *n* = 7). Figure partially created in BioRender. Flaherty, S. (2026) https://BioRender.com/5untbr3.

Figure 8 Ketamine inhibits the inverse haemodynamic response to spreading depolarizations. (**Ai)** DC-ECoG and rCBF (PU) traces from saline and ketamine (15 mg/kg) injected animals after 1st 60 s photothrombosis (control) and after 2nd 180 s photothrombosis. Green bars illustrate illumination time and black arrow marks time of vehicle administration. (A**ii**) rCBF traces from saline and ketamine injected animals displaying example CSD-induced haemodynamic responses at similar normalised perfusion ranges (PU). Black dashed lines mark the start of the CSD. (**B)** Mean CSD-induced haemodynamic response type from saline and ketamine injected animals following 180 s photothrombosis (saline group 348 events, *n* = 11; ketamine group 345 events, *n* = 6). (**C**) Final resting (minimal influence from CSD induced perfusion changes) rCBF (PU) in function of distance to lesion core (mm) quantified 1.5 hours following 2nd 180 s photothrombosis from saline and ketamine injected animals. (**D**) Quantification of normalised perfusion (PU) against distance (mm) to lesion core (saline group 198 ROIs, *n* = 15; ketamine group 110 ROIs, *n* = 7). Plot compares CSD 3 from saline and ketamine injected animals. **(Ei)** Example cresyl violet staining of a mouse brain following PT induction with either saline or ketamine administration 24 hrs post ischaemia induction. **(Eii)** Comparison of infarct volume (mm^3) between saline and ketamine injected animals following PT (saline 14.5 ± 1.8 mm^3, ketamine 7.1 ± 2.0 mm^3, t-test, **** $p < 0.001$). Vehicle was injected 5 s before the second 180 s illumination. Figure partially created in BioRender. Flaherty, S. (2026) https://BioRender.com/05qbmn4.

ACCEPTED MANUSCRIPT

Downloaded from academic.oup.com/brain/advance-article/doi/10.1093/brain/awag305/8788779 by guest on 24 November 2026

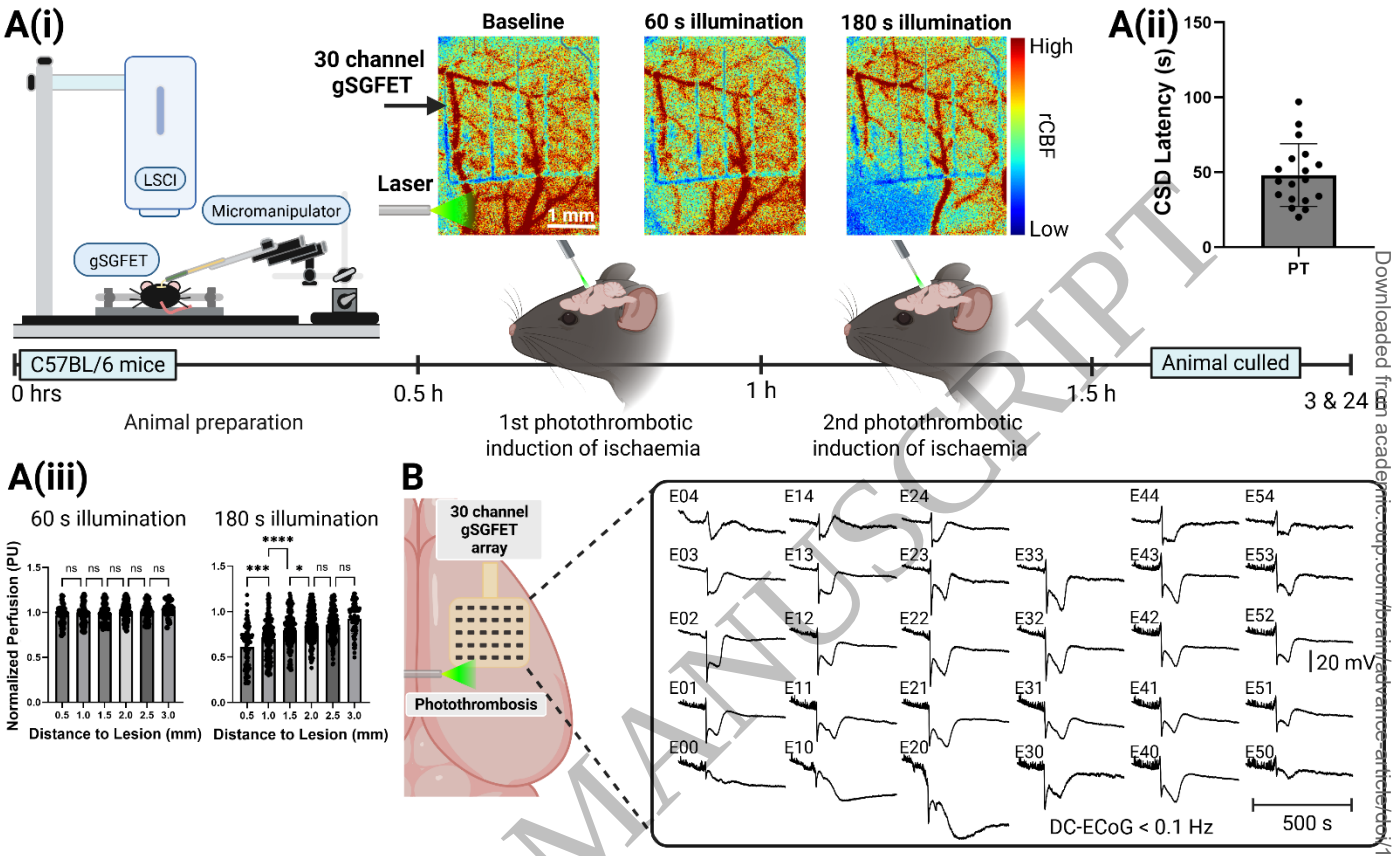

Figure 1
185x116 mm (x DPI)

ACCEPTED MANUSCRIPT

Downloaded from academic.oup.com/brain/advance-article/doi/10.1093/brain/awag305/8788779 by guest on 24 November 2026

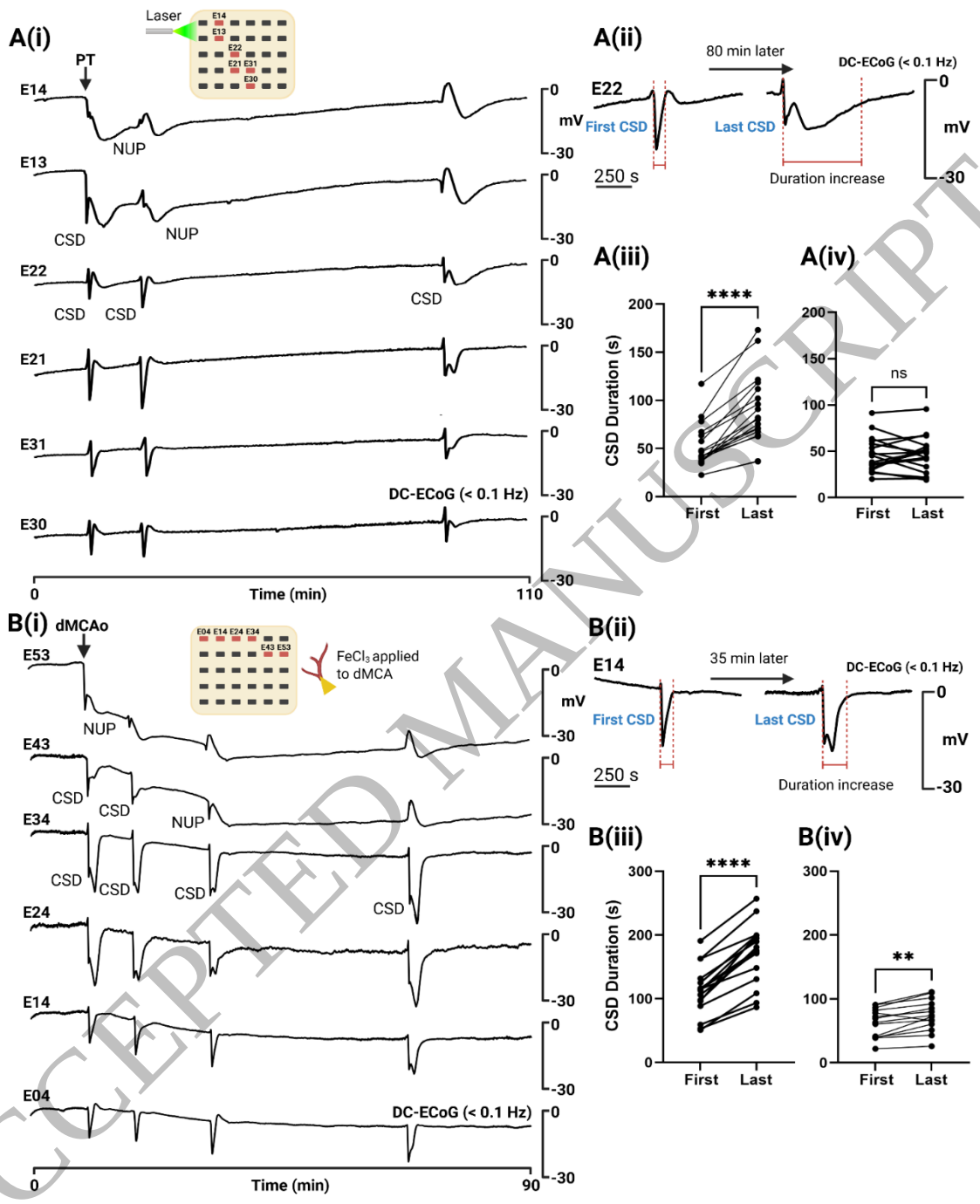

Figure 2
185x240 mm (x DPI)

ACCEPTED MANUSCRIPT

Downloaded from academic.oup.com/brain/advance-article/doi/10.1093/brain/awag305/8788779 by guest on 24 November 2026

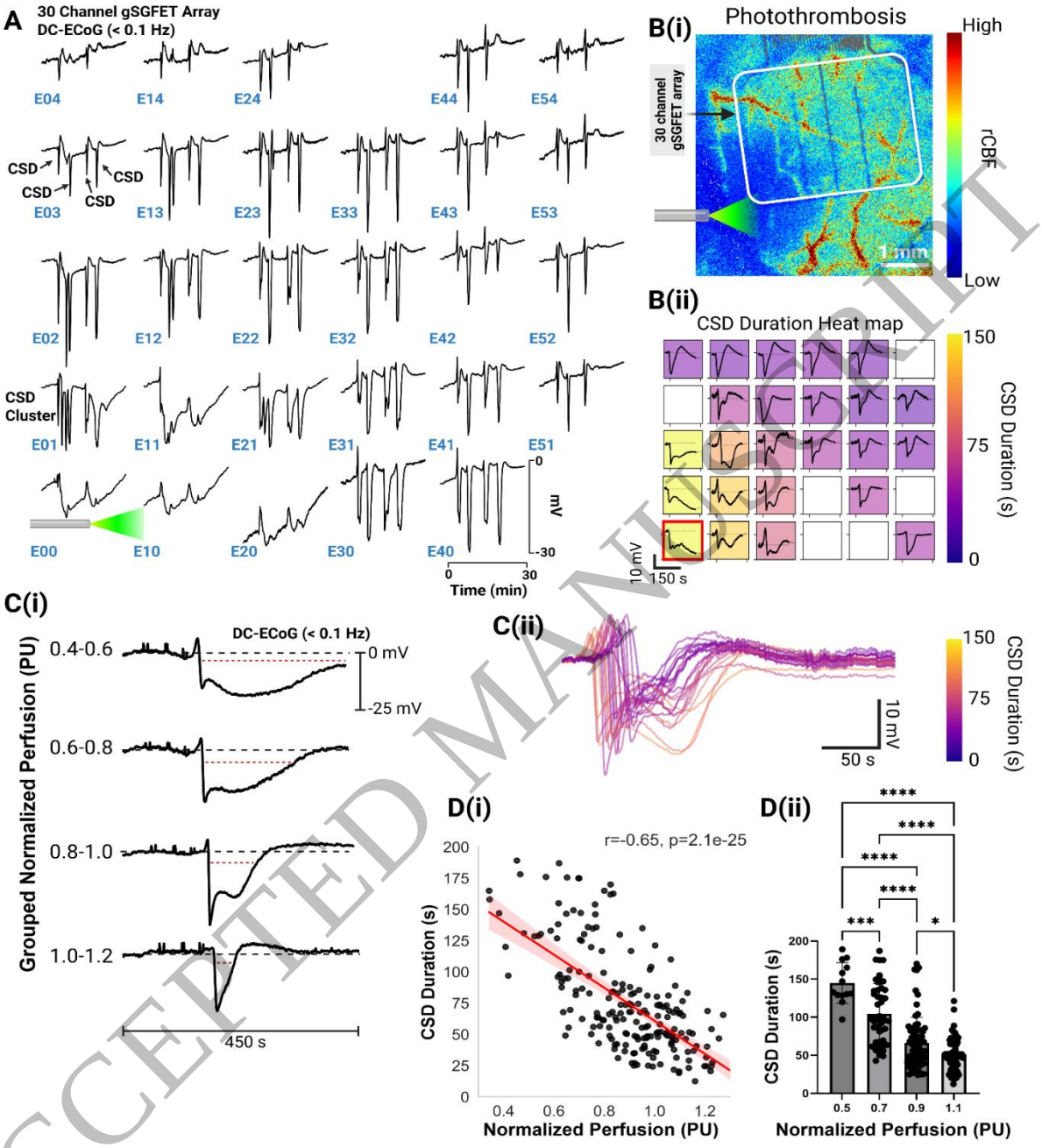

Figure 3
185x219 mm (x DPI)

ACCEPTED MANUSCRIPT

Downloaded from academic.oup.com/brain/advance-article/doi/10.1093/brain/awag305/8788779 by guest on 24 November 2026

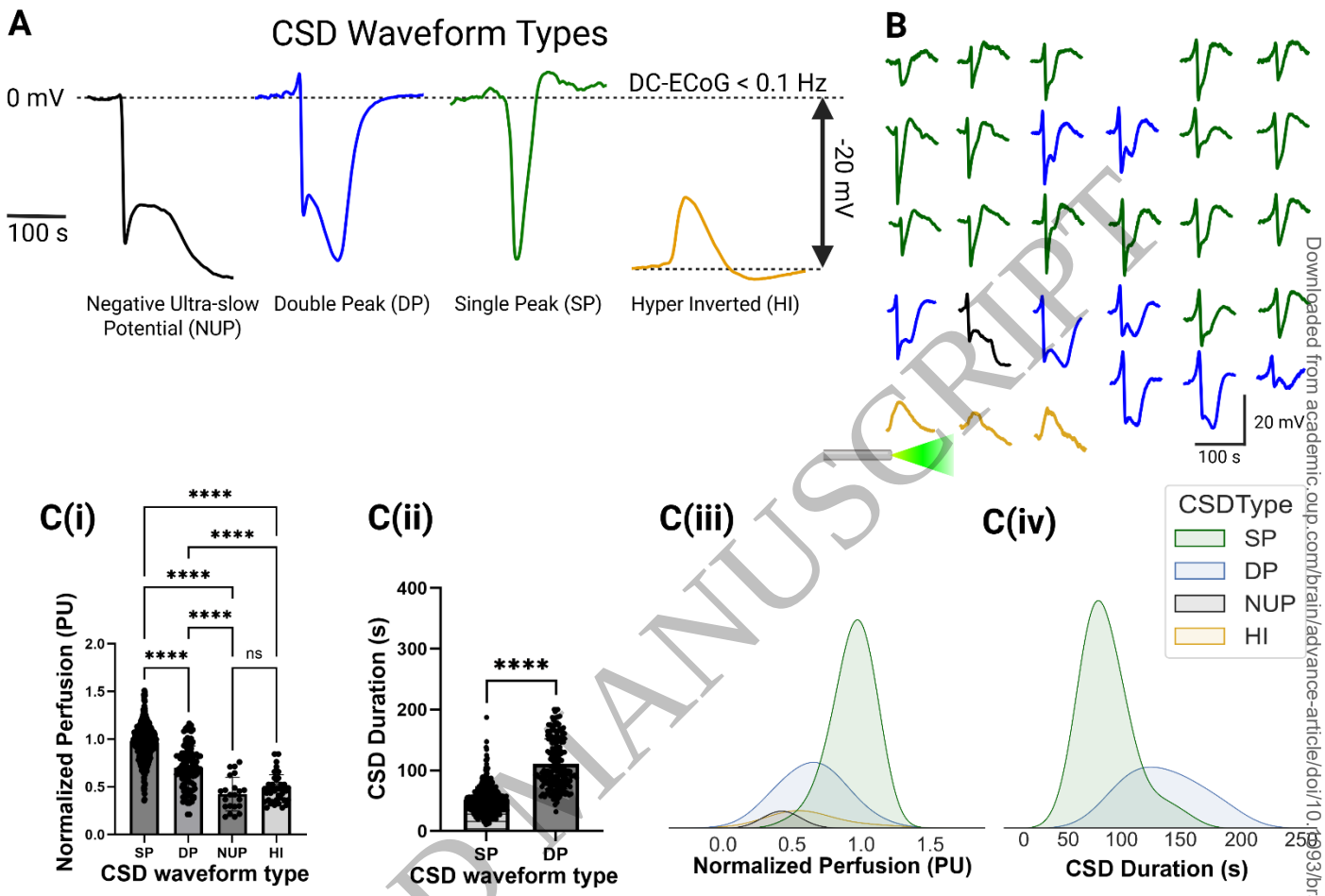

Figure 4
185x127 mm (x DPI)

ACCEPTED MANUSCRIPT

Downloaded from academic.oup.com/brain/advance-article/doi/10.1093/brain/awag305/8788779 by guest on 24 November 2026

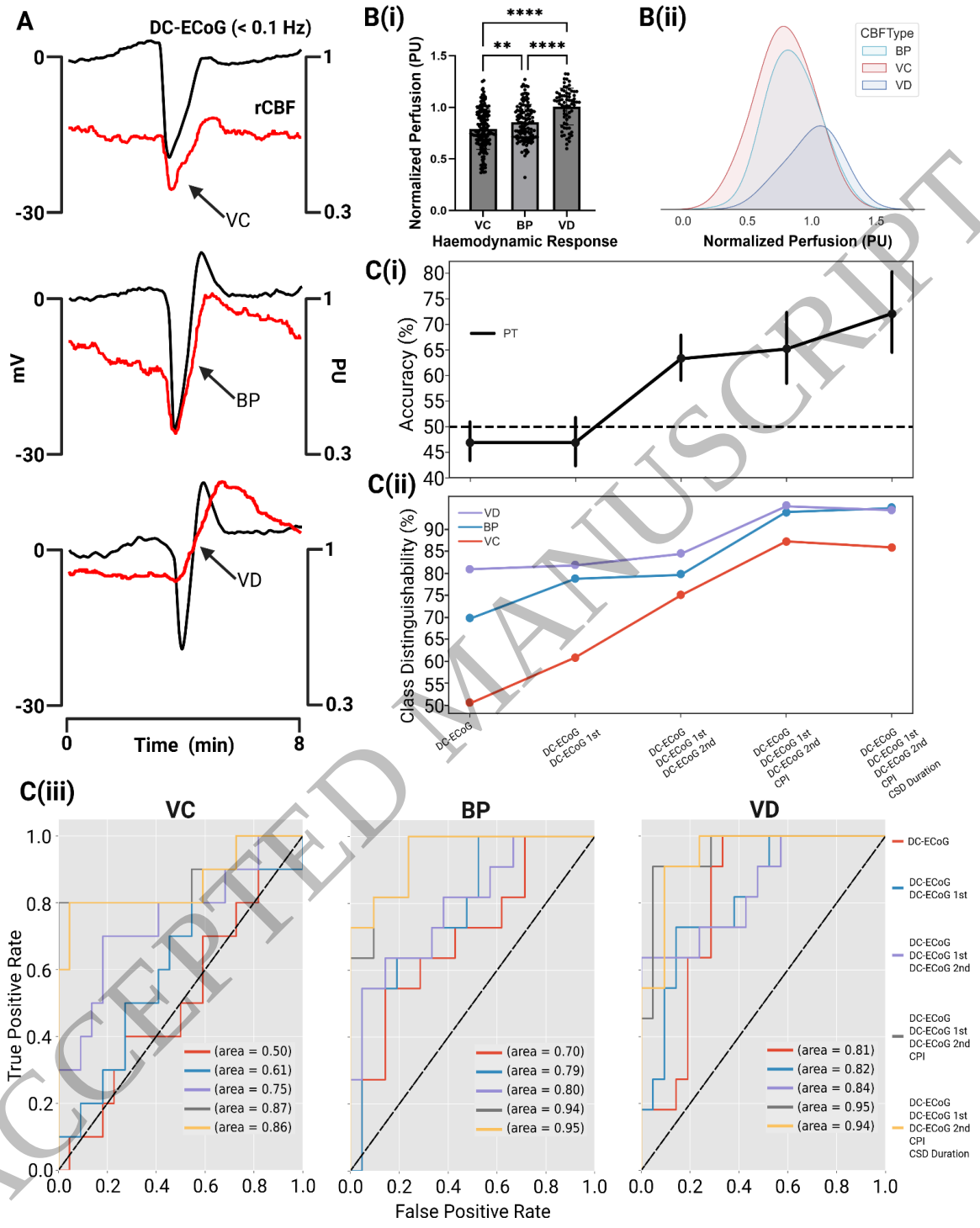

Figure 5
185x230 mm (x DPI)

ACCEPTED MANUSCRIPT

Downloaded from academic.oup.com/brain/advance-article/doi/10.1093/brain/awag305/8788779 by guest on 24 November 2026

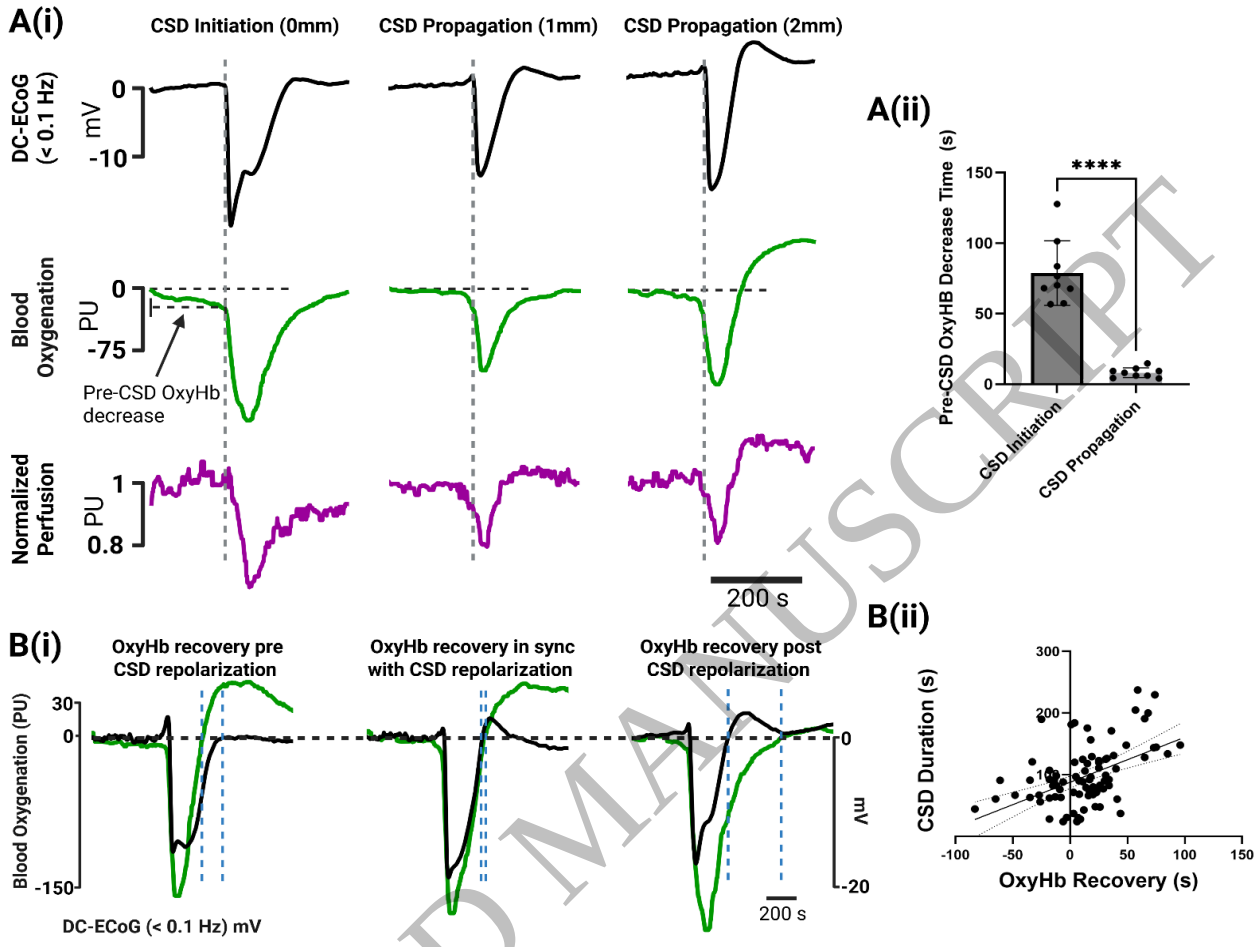

Figure 6
185x143 mm (x DPI)

ACCEPTED MANUSCRIPT

Downloaded from academic.oup.com/brain/advance-article/doi/10.1093/brain/awag305/8788779 by guest on 24 November 2026

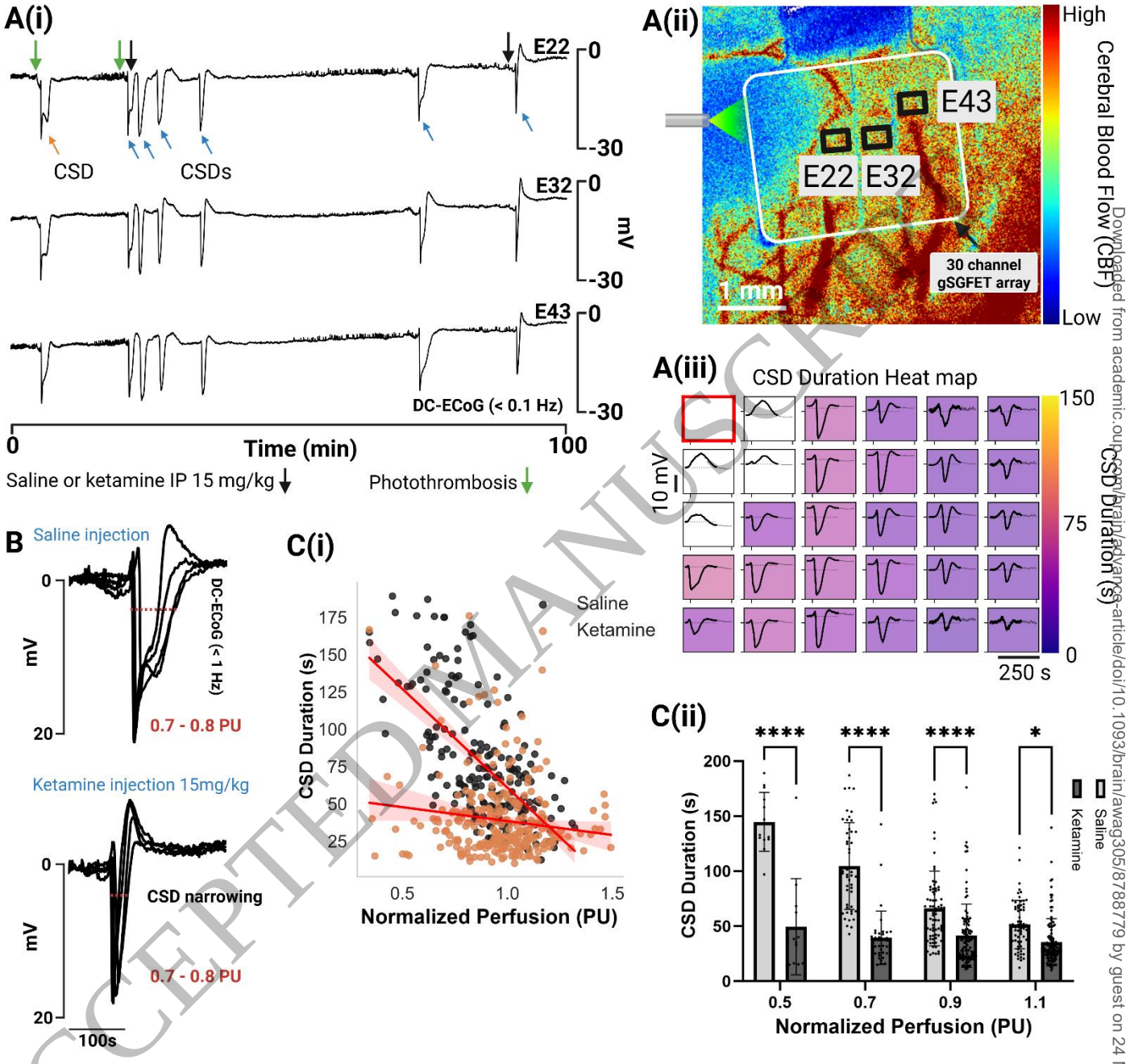

Figure 7
185x174 mm (x DPI)

ACCEPTED MANUSCRIPT

Downloaded from academic.oup.com/brain/advance-article/doi/10.1093/brain/awag305/8788779 by guest on 24 November 2026

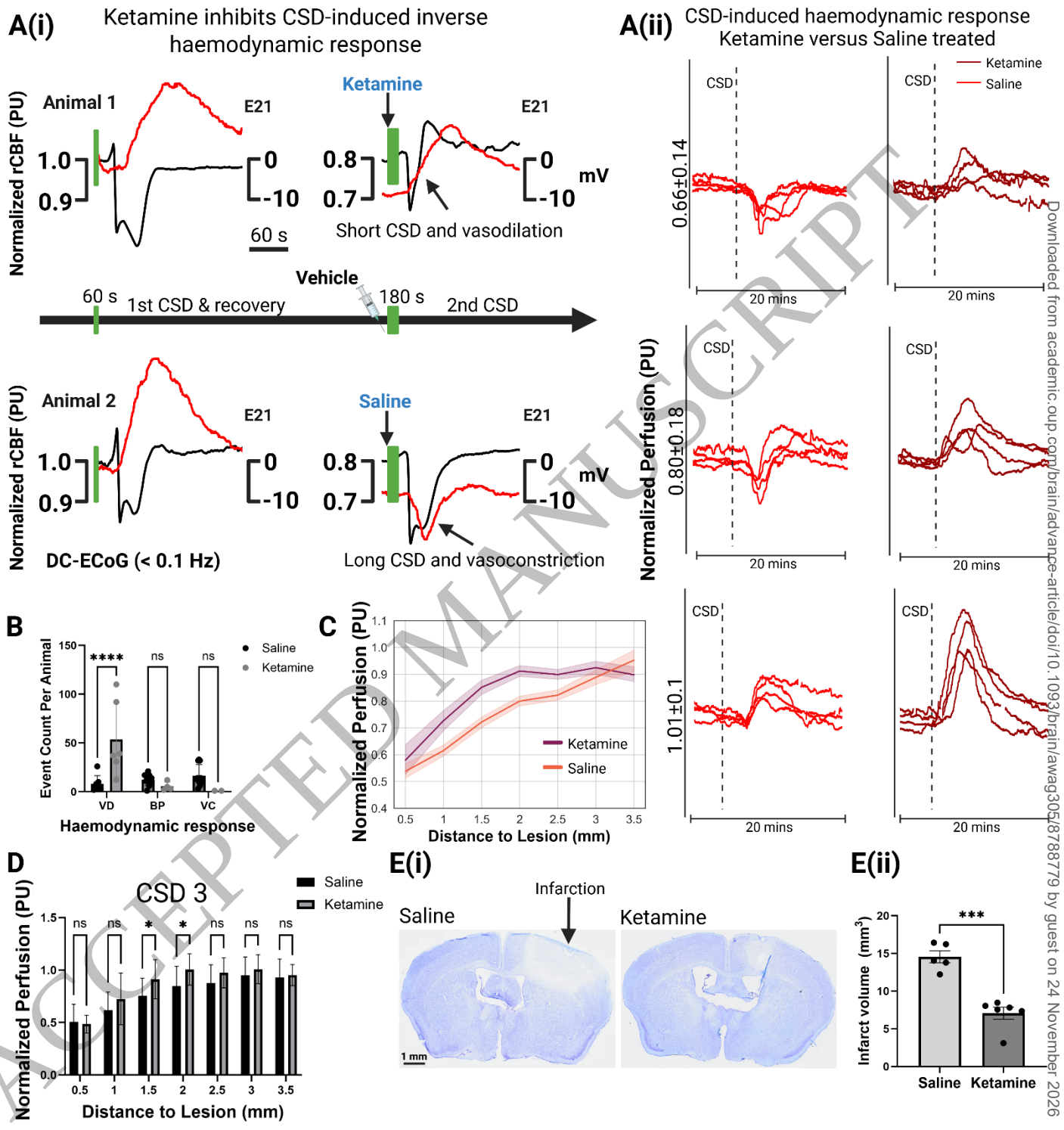

Figure 8
185x196 mm (x DPI)

ACCEPTED MANUSCRIPT

Downloaded from academic.oup.com/brain/advance-article/doi/10.1093/brain/awag305/8788779 by guest on 24 November 2026